CHAPTER 2

Notions for the Motions of the Oceans

Baylor Fox-Kemper

Dept. of Earth, Environmental, and Planetary Sciences, Brown University, Providence, RI, USA

Operational oceanography combines models and observations to assess and predict the ocean state. While the mechanisms of forcing and equations of fluid motion for the ocean are known, present computers cannot solve all of the relevant scales of motion at the same time. Thus, choices of scales to emphasize must be made in operational systems. This chapter explores some of the issues in choosing a scale, including evaluating approximations to the equations of motion, typical kinds of variability at different scales, and parameterizations of unresolved processes.

Introduction

Operational oceanography aspires to combine observations with models to infer and predict the state of the oceans. Which aspects of the ocean state are of interest vary by application, but almost always it is important to know the basic physical properties: where we expect the water to be and where it is moving. Biological and chemical predictions rely on these physical basics and sometimes can affect the physics (e.g., through limiting solar illumination at depth), but the focus of this chapter will be on the physical aspects: our notions for the motions of the oceans. Ocean motions result from the overall forcing of the climate system (first section), but are filtered through a variety of processes on different scales before arriving at the motions of interest for a particular application (third and fourth sections). For example, an oceanic mesoscale eddy has the same area as about 1-10 Rhode Islands (0.85 to 8.5 Mallorcas), but the dissipation processes that ultimately remove the energy that energizes the 1-2 year eddy lifetime occur on the scale of millimeters. Operational oceanography follows an even grander vision–not only to infer the motions but to make them amenable to applications. They are the building blocks needed for practical questions such as: “What is the best way to get where I’m going on my sailboat?”, “Where are the fish today?”, “What marine ecosystems are most vulnerable to climate change?”, “When is high tide here?”, “Are there seamounts or oil on the seafloor here?”, and “Are submarines hiding near my naval fleet?

An ocean model is a combination of the state variables that describe the ocean state, their interrelationships (i.e., the equations of motion), key physical parameters (e.g., the gravitational acceleration near the Earth’s surface), and external forcing at the simulation boundaries (e.g., winds, rivers, runoff, air-sea energy and mass exchange, and precipitation – all of which are inferred from observations, other models, or climatology). As the relationships tend to be complex mathematically, we normally formulate and “solve” a model using computers. A model “solution”

Fox-Kemper, B., 2018: Notions for the motions of the oceans. In "*New Frontiers in Operational Oceanography*", E. Chassignet, A. Pascual, J. Tintoré, and J. Verron, Eds., GODAE OceanView, 27-74, doi:10.17125/gov2018.ch02.

or "simulation" in the absence of observations is just an integration of the initial and boundary condition problem over a window of time. A data-assimilating model "solution" is similar, except that ocean observations are used to realign the simulation toward the observed ocean state, which may require multiple iterations of running and readjusting the model initial and boundary conditions, a series of backwards and forward integrations between each time of observation, or just steps in the integration where the equations of motion are violated or "nudged" to adjust the model state toward the observations. Observations may be used just for forcing and checking the state prediction, which can be called *vetting a forward model*, or observations may be used with an inverse model designed to infer which ocean states are consistent with the constraints of observations collected. In a hybrid approach, data is *assimilated* into a model through the steps outlined above and detailed in other chapters of this book.

The fundamental constraints on the physical and physical-chemistry aspects of seawater have been well understood for more than a century, and they are encapsulated in the conservation equations describing the motion and evolution of seawater. However, these equations are difficult to solve exactly, and even their approximated, discretized form (e.g., on a model *grid*) requires significant computational effort.

Thus, either the scope in terms of domain or duration of the ocean state predicted by the model or the degree of detail captured in its discrete form (the grid *resolution*) is limited. Likewise, observations are limited in scope, accuracy, and precision because getting out on and into the water is expensive and hazardous. Management of the limitations of computation, observations, and understanding to provide the best ocean state prediction is the central challenge of operational oceanography.

This chapter presents the framework and many known aspects of oceanic motions over the scales from global to microscopic that delineate the management of these limitations. The unifying theme will be examining the equations of motion on a variety of scales, together with a few key descriptors of fluid motions at important scales, intended to convey what approximations to the equations are useful in modeling practice and where the near future may take us.

What Drives the Motions of the Oceans?

Early after the Earth formed, its surface was still hot from the gravitational potential energy released during the accretion of Earth-stuff out of the early solar system. The late impact that created the Moon warmed things up again, and the nuclear decay by fission of radioactive elements and continuing release of latent heat as the liquid core solidifies contribute extra sources of energy. A little less than 0.1 W/m^2 of this geothermal energy escapes the seafloor on average. The Sun, on the other hand, uses nuclear fusion as well as fission. Fusion provides the sun with a mechanism and fuel to continue to radiate energy brightly for billions of years.

Kelvin estimated the age of these celestial bodies, based on the rate of cooling and their initial energy source, but his estimate was about ten times younger than geologists estimated Earth's sediments to be! Puzzling through the age of the Earth and Sun helped push forward geology and physics. Known as Kelvin's age of the Earth paradox, this discrepancy was one of earliest applications of the conservation of total (thermal and mechanical) energy in astrophysics and geophysics (Richter, 1986; Stacey, 2000).

Fusion keeps the solar system warm, so presently the vast majority of the heating of the Earth and thus the motions of the atmosphere and oceans comes from the Sun's energy (Fig. 2.1a). At the top of the atmosphere, 341 W/m^2 of solar power arrives as primarily shortwave radiation, and about 102 W/m^2 of this shortwave radiation is reflected back to space. Infrared radiation, emitted by varying sources throughout the earth system, sends about 239 W/m^2 back to space. The brightness temperature, or the temperature that would produce this amount of outgoing infrared radiation by the Stephan-Boltzmann law, must be 255 K for the Earth as a whole to achieve 239 W/m^2. However, the satellite observed brightness temperature varies from around 190 K to about 320 K, reflecting variation in the latitude, altitude, and components of the earth system (clouds, atmosphere, upper ocean, land, ice) that are responsible for the infrared emissions. Radiation from lower altitude emitters has to penetrate the shield of greenhouse gasses of the atmosphere (mainly water vapor, ozone, carbon dioxide, methane, and nitrous oxide). These species of gasses are identified as part of the "greenhouse" effect because they are special in their tendency to absorb infrared radiation, blanketing the earth with an insulating layer that warms the surface to a comfortable average of 288 K. Global warming, or the effects of human-induced, or *anthropogenic*, emissions of additional greenhouse gasses is a primary reason why the average temperatures in 2016 and 2017 were 0.94 K and 0.84 K above the 20th century mean of 287.0 K (NOAA, 2018). Overall, the integrated energy budget of the Earth is very nearly in balance at the top of the atmosphere, at least when averaged over a few decades of variability and aside from the systematic small imbalance due to anthropogenic greenhouse gasses (Trenberth and Fasullo, 2010; Hansen et al., 2011). The small imbalance is most readily detected by ocean warming and sea level rise–key targets for operational oceanography (Von Schuckmann et al., 2016).

But latitude-by-latitude, the energy budget is not in balance (Fig. 2.1b). The equator and tropics receive an excess of incoming radiation over outgoing, while the extratropics and polar latitudes emit more energy back to space than arrives from the Sun. Fig. 2.1b represents the annual average as estimated from satellites and atmospheric data by Trenberth and Caron (2001). As the seasons change or as day turns to night, the balance between incoming and outgoing radiation changes latitude-by-latitude and longitude-by-longitude (or timezone-by-timezone).

Consider the amount of power associated with these variations, roughly 100 W/m^2 over the seasons and 500 W/m^2 day versus night. The specific heat capacity of dry air is 1 J/gK and of seawater is 4 J/gK. The hydrostatic pressure at 10 m ocean depth is about 2 atmospheres–1 from the weight of the atmosphere and one from the weight of the ocean. Thus, ten meters of seawater weighs the same as the whole atmosphere above it (10^4 kg/m^2). Using this weight to estimate their relative masses, the atmosphere has a total heat capacity near 10^7 J/m^{2}K–equal to about 3 meters of seawater. More precisely, a dry atmosphere has about the same heat capacity as 2.5 m of seawater, but if water vapor (specific heat capacity of 2 J/gK) is included a typically moist atmosphere has the same heat capacity as about 3.4 m of seawater–so let's just remember 3 m. If 100 W/m^2 heating is applied to either the atmosphere or 3 m of the ocean, they would warm at 10^{-5} K/s, or a bit more than a degree Kelvin per day. In Providence, day-to-night temperature swings are about 5 K, which is consistent with removing the solar input of energy with this atmospheric heat capacity. Winter-to-summer warming is about 20 K over 6 months–a much slower rate due to the more subtle changes in sunlight over the seasons, but more importantly due to the amelioration of warming and cooling by the heat capacity of the roughly 50 m ocean mixed layer–which has an order of magnitude more heat capacity than the atmosphere. Melting ice and evaporating water takes 84 and 560 times as much energy as warming the same mass of water by 1 K, thus even though there are only a few meters worth of evaporation, precipitation, and formation of sea ice these terms contribute at leading order to the overall energy budget. However, this power analysis is still only providing a vertical picture of the energy exchanges, when understanding the forcing of the climate system requires appreciating the meridional gradients as well.

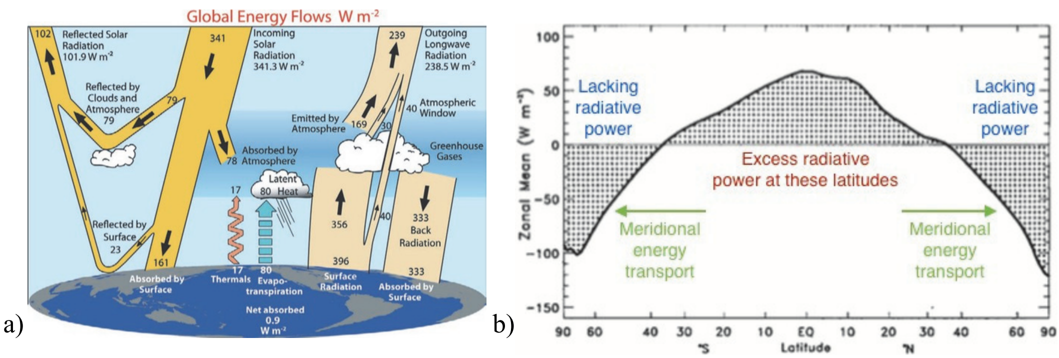

Figure 2.1. a) Estimated flows of energy through the earth system, based on observations from March 2000 to May 2004 (Trenberth and Fasullo, 2009). b) Annual mean top of atmosphere net radiative power (i.e., incoming minus outgoing) by latitude, schematized to indicate meridional energy transport (adapted from Trenberth and Caron, 2001).

The large heat capacity of the ocean makes its temperature changes less sensitive to brief variations in forcing and also makes it the dominant reservoir of thermal energy in the earth system. Thus, the global warming signal is less noisy when detected in ocean warming even though ocean measurements (by ship, buoy, etc.) are practically challenging (Von Schuckmann et al., 2016), and it is the reason why atmospheric variability is "reddened", or reduced at high frequencies versus low frequencies, by the ocean in the coupled system (Frankignoul and Hasselmann, 1977). Thus, on large scales, the variability of the atmospheric weather is dampened and less detectable in ocean temperature changes. On small scales, ocean eddies–the dynamical equivalent of atmospheric weather–produce variability that can drive the atmosphere above (Frenger et al., 2013).

As Fig. 2.1b shows, different latitudes receive an excess of radiative power while others receive a deficit. If the whole system is to be in balance, there must be an exchange of energy between the excessive regions toward the deficient ones. A maximum of about 5.7 PW of poleward energy transport in each hemisphere is needed near 40° where the zero-crossings in Fig. 2.1b are. There are three primary mechanisms by which energy is transferred. Only a negligible amount of potential or kinetic energy is transported (Peixoto and Oort, 1992), so the three primary mechanisms are sensible heat transfer in the atmosphere, sensible heat transfer in the ocean, and latent heat transfer in the coupled system.

First, the atmospheric sensible heat transport is carried by warm air moving poleward on average and colder air moving equatorward, which carries a maximum of about 3 PW. The Hadley Cells ascend near the equator to the tropopause and move poleward to about 30° where they descend and return back toward the equator. The upper branch carries warm air poleward and the lower branch carries cold air southward, thus a net poleward exchange of sensible energy. Because the air in the Hadley cell is heated at low altitudes/high pressure and cooled at high altitudes/low pressure, there is a conversion of thermal energy to mechanical energy that drives the Hadley cell, much like a Carnot cycle (Pauluis, 2011). The Polar Cells, which circulate poleward of about 60° exhibit similar thermally direct overturning. Importantly, these cells do not move directly from equator to pole, but are veered by the Coriolis force, so they have dominantly zonal winds at the surface. The equatorial easterlies and midlatitude westerlies are a consequence of such veering.

Second, the oceanic sensible heat transport is carried by warm seawater moving poleward on average and colder seawater moving equatorward, and it moves a maximum of about 2 PW poleward when zonally integrated over all ocean basins (Trenberth and Caron, 2001). In old-fashioned thinking this *thermohaline circulation* was thought to result from the formation of North Atlantic Deep Water (NADW) or Antarctic Bottom Water (AABW) by cooling & increasing salinity at polar latitudes and heading equatorward at depth. These waters are resupplied by warmer water at the surface, thus there is a transport of sensible heat poleward. However, modern analyses have revealed that this picture is too simple for a number of reasons. Firstly, the oceans are heated and cooled at the surface which means that unlike the atmosphere they cannot extract mechanical energy for circulation as a heat engine or Carnot cycle, because heating and cooling occur at the same pressure.[1] Thus, the energy for the circulation cannot result from the thermal forcing–instead it must come from other sources, e.g., winds and tides. Secondly, the direction of the ocean heat transport is not consistent with this thermally-driven picture. The oceanic meridional heat transport is poleward when zonally-averaged over the whole Earth, but the Atlantic Ocean heat transport is northward at all latitudes—even in the Southern Hemisphere--and the Indian Ocean heat transport is southward at all latitudes (Trenberth and Caron, 2001). Thus, the ocean circulation is not everywhere consistent with poleward heat transport, and regional transports reflect important variations in currents. Thirdly, the old notion of a *wind-driven* circulation and a separate thermohaline circulation is not sensible as these two mechanisms are not distinct. The more modern concepts of a *Meridional Overturning Circulation* (MOC), which can be driven by any force but overturns (after zonal integration) in the meridional-vertical plane can be cleanly distinguished from a gyre, or *barotropic circulation*, that circulates in the zonal-meridional plane after vertical integration. The MOC and barotropic circulations are distinct in terms of volume transport. However, *both* of these circulations contribute to oceanic meridional heat transport. The NADW &

[1] Solar radiation that penetrates about 100 m depth and geothermal heating at the seafloor versus sensible at latent cooling right at the ocean surface, as well as meridional variations in atmospheric pressures due to the circulation, are modest exceptions to heating and cooling at equal pressure.

AABW are good examples of branches of the MOC, but so too are the Subtropical Cells (STC)--wind-driven upper ocean cells importantly related to equatorial Ekman upwelling and zonal winds.

Third, the atmosphere/ocean latent heat transport is moist air moving poleward and dry air and liquid water in oceans and rivers moving equatorward, and it moves a maximum of about 1 PW poleward (Peixoto and Oort, 1992). In this exchange of water, the latent heat of vaporization is transported from the location where evaporation occurs to where the precipitation occurs. Pauluis (2011) notes that this "steam cycle" transport generates mechanical energy much like a steam engine. As already noted, it takes 560 times as much energy to evaporate water as to warm it by one degree, so even though the hydrological cycle transports only a small mass of water (about 1 Sv) compared to ocean currents (about 40 Sv in global MOC) or atmospheric winds (about 60 Sv in the Hadley Cells), it carries a lot of heat.

It is a fascinating aspect of the earth system that the transport of heat and moisture by the three mechanisms above may differ significantly between the mean mass transport and the mean heat and moisture transport. At latitudes between 30° and 60°, transient storms carry enough warmth and moisture intermittently to reverse the direction of the air mass transported by the Ferrel Cells, which are the average circulations at these latitudes (Peixoto and Oort, 1992; Held and Schneider, 1999). Similarly, Southern Ocean eddies reverse the heat transport to oppose the mass transport in the Deacon Cell (Karsten and Marshall, 2002).

Celestial forcing, including seasonal and diurnal as well as longer timescale orbital variations, change these energy budgets temporarily. For example, peak Northern Hemisphere winter atmospheric sensible plus latent transport exceeds 8 PW. Climate variability can also alter these patterns. For example, a large El Nino can change the meridional energy exchanges significantly and flush out excess energy in the upper ocean (Sun and Liu, 1996; Deser et al., 2006).

Overall, the ocean receives most of its energy near the global scale, due to the global scale of solar input (and thus winds) and the global scale of tidal forcing. In total, the amount of kinetic energy forced to occur in the oceans is about (24 TW=2.4×10^{13} kg m^2/s^3 from Wunsch and Ferrari, 2004) – only a small fraction of the imbalance in solar forcing.

The climate system has periodic forcing and resonances with a given period, but also broad-banded turbulent variability. The timescales of forcing are precise for the celestial forcing: tidal, diurnal, and seasonal. Atmospheric forcing timescales have to do with weather, which is a chaotic and turbulent process with broad-banded variability rather than discrete periods, and the ocean's greater heat capacity means that atmospheric-forced ocean variability has a preference for lower frequencies. On smaller length scales and longer timescales ocean eddies may drive the atmosphere, again in a chaotic and turbulent process without countable frequencies. Another source of useful timescales for the ocean is the time required for waves to cross basins of a particular dimension. These crossing timescales govern the *resonance* of ocean basins to tidal and seasonal forcing and also set the adjustment timescale of a basin to perturbations. Thus, although tidal forcing is global, the strongest responses (e.g., Bay of Fundy, English Channel) are in basins where the wave crossing timescale matches the period of a tidal forcing. Coupled phenomena, such as El Nino with its 2 to 7 year repeat timescale, are informed by ocean wave crossing timescales but also retain relatively broad-banded variability due to the chaotic nature of atmospheric forcing and response. The next section will clarify some of the notions of spatial and temporal scale for the ocean's motions.

Scales of named oceanic motions

The largest length and longest timescales on the Earth are the circumference of the Earth (4.0x10^7 m) and Earth's age (4.54x10^9 years=1.43x10^{17} s), which set the top and right bounds of Fig. 2.2, but most ocean variability occurs on smaller scales. The ocean is subdivided into basins which change slowly by plate tectonics, but usually these changes are neglected because they are too slow to resonate with an oceanic response. Fast tectonic changes (i.e., earthquakes), do lead to tsunamis, which are among the fastest propagating oceanic signals. The speed of sound is a bit faster, which sets the bottom limit of Fig. 2.2. The slowest ocean and climate variability is normally taken to be paleoclimatic responses (e.g., ice ages) to the variability in Earth's orbit (Milankovitch, 1930). These largest scales define the upper limits in Fig. 2.2.

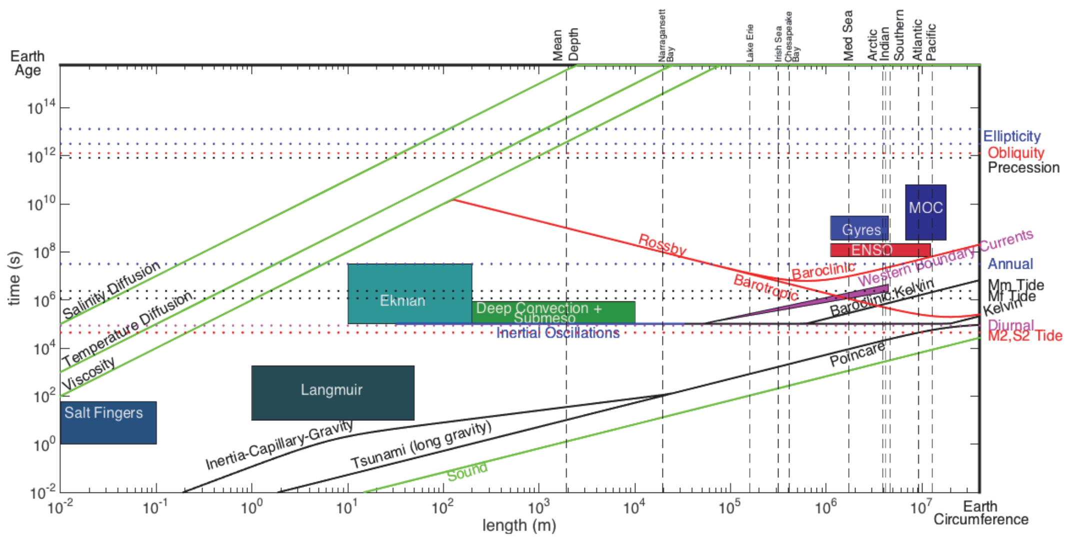

Figure 2.2. Taken from Haidvogel et al. (2017): Approximate length and timescales of oceanic motion, showing many wave dispersion relations–that is, the relationship between timescale and lengthscale of each type of waves–the scaling of viscous and diffusive motions, and the length and timescales of basins and common forcing mechanisms. A latitude of 25° is used to estimate Coriolis parameters.

The smallest scales of *fluid* motion, which might be taken to bound Fig. 2.2 on the left, are the scale of separation of water molecules or the mean free path of a moving molecule of water before it interacts with another, both of which are a few Å or $O(10^{-10}$ m). In a numerical model, however, we normally accept that once the *dissipation scales* of fluid motion, which are the smallest scales of turbulent variability, are resolved then the simulation is accurate and is called a *Direct Numerical Simulation* (DNS). Kolmogorov (1941) theorizes these smallest scales of dissipative motion to be $\nu^{3/4}\epsilon^{-1/4} \approx 0.3$ cm for length and $\nu^{1/2}\epsilon^{-1/2} \approx 10$ s for time. In this estimate the kinematic viscosity of seawater is taken as $\nu \approx 1 \times 10^{-6}$ m^2/s. The kinetic energy dissipation rate per unit mass, E, varies by about 4 orders of magnitude throughout the world (Waterhouse et al., 2014; Pearson and Fox-Kemper, 2018), but it can be roughly yet directly estimated to be $O(10^{-8}$ m^2/s$^3 = 10^{-8}$ W kg$^{-1})$

using the total energy input to the ocean (24 TW=2.4 10^{13} kg m^2/s^3 from Wunsch and Ferrari, 2004) divided by the ocean mass of 1.4 10^{21} kg, under the possible oversimplification that the fraction lost to potential energy by mixing and the fraction lost by waves lifting beach sediments, etc., do not change the order of magnitude of the kinetic energy. The scales of temperature and salinity diffusion are a bit slower or smaller than those of kinetic energy dissipation (Obukhov, 1949; Corrsin, 1951, Fig. 2.2). Finally, as waves tend to oscillate faster than turbulence overturns, waves lead to considerably faster timescales than the turbulent estimate of 10 s. For example, the sound waves in a typical blue whale song are a hundred times faster, with a fundamental frequency of 10 to 40 Hz. Generally, larger scale motions are slower than smaller scale ones, with the intriguing exception of barotropic Rossby waves (Fig. 2.2) where graver modes are able to sense larger variations in the curvature of the Earth and are speedier.

Fig. 2.2 also indicates rough ranges for other types of oceanic motions of interest. A range of overturning scales for branches of the Meridional Overturning Circulation are indicated, as is the El Nino/Southern Oscillation, the circulation timescale and wave crossing timescales of gyres (at the intersections of waves with basin dimensions), and the depth and timescale of the Ekman (1905) layer, etc. Note that all of these phenomena lie in the region of scales between viscosity, sound waves, Earth's circumference, and Milankovitch (1930) forcing of ellipticity. This is the phase space domain of oceanography on Earth, from which an ocean simulation spanning a particular range of scales might be chosen.

Reduced Models

Much is known about the equations governing the motions of the oceans. Practical approximations to the equations are known for all of the named ocean phenomena shown in Fig. 2.2. Improvements are still possible, however, which seek to better incorporate the effects of unresolved scales of motion through *parameterizations*. The small scales in Fig. 2.2 have been directly studied in the laboratory, so their behavior is well-known and may be directly simulated in small domains. On these scales, the equations of motion have been long known (Éuler, 1757; Laplace et al., 1829), and effective phenomenological laws can be formulated to capture the bulk behavior of molecular motions assuming *local* thermodynamic equilibrium (Fourier, 1822; Fick, 1855; Navier, 1822; Stokes, 1845; Onsager, 1931a,b). First, let's examine the limits of computation, then return to approximations that make the equations of motion less expensive to solve.

Reduced to fit computational limits

Present computing capabilities can be quantified in units of a *tera-grid*, which is the computational equivalent of 10^3 discrete steps in each of the 3 spatial directions and time, for 10^3 x 10^3 x 10^3 x 10^3 = 10^{12} unique spatio-temporal locations, or a tera(10^{12})-grid. A typical graduate student computational project might be a few teragrids in computational cost, while present grand challenge simulations are about a hundred teragrids. As the ocean is relatively shallow on average (3.7 x 10^3 m) compared to its horizontal dimension (4.0 x 10^7 m), often many more degrees of freedom are used in the horizontal rather than vertical direction. Resolving the stratification of water properties does require somewhat finer vertical resolution than this purely geometric scaling. Paleoclimate applications can require long duration simulations to rival the Milankovitch (1930) timescales, which necessitates fewer spatial grid points in the horizontal and vertical.

In Fox-Kemper et al. (2014), it is shown that the empirical exponential increase in computing power (Moore, 1965) has resulted in an empirical exponential refinement of ocean model grid scale for climate modeling applications. Moore's observed increase in computation predicts a doubling of model resolution– halving all grid spacings and time step–every 6 years. In practice, models become increasingly complex as well as refined, so the observed resolution doubling rate is closer to 6.9 years for basic atmosphere-ocean models and 10.2 years for complex earth system models. At the basic rate, we will leave behind the now typical ocean tera-grid for a peta-grid in about 18 years. Thus, an undergraduate can expect to exceed today's most computationally-costly simulation on a regular basis as a senior scientist. Looking to the past, the first weather simulation used a deca-kilo-grid (Charney et al., 1950), and from this datum the basic rate of increase predicts reaching a tera-grid in 61 years. However, the first weather run was a grand challenge taking the whole of the fastest computer available for 24 hours, including a daunting output of 100,000 punch cards of data! The output of a tera-grid calculation today is more manageable–saving every 20th time step for 5 ocean state variables (u, v, w, S, T) on a tera-grid at single precision requires only 1 terabyte, although this quantity of data was a considerable challenge about a decade ago (e.g., Maltrud and McClean, 2005). It is important to note that computing power, data storage, and internet connectivity do not accelerate at the same exponential rates, so mismatches are likely to limit future ocean models. The capability to simulate a basin filled with mesoscale features in models and satellite observations shifted the focus of oceanography in the 90s, as resolving basins full of submesoscale phenomena is now. The historical pattern is that resolution increases sufficient to qualitatively change ocean simulations occur slowly but surely, averaging a handful of times in a scientist's career.

The problems studied in operational oceanography vary in scope, but present forward global models at 2 km horizontal resolution have been run for a few years (Rocha et al., 2016a,b). This massive calculation has $O(10^{10})$ wet grid points, so a tera-grid is reached in only 100 time steps. The additional costs of data assimilation mean that operational regional coastal ocean forecast systems have similar horizontal grid scales (Kourafalou et al., 2015), while regional and idealized forward models may have much finer resolutions, from hundreds of meters to meters (Hamlington et al., 2014; Haney et al., 2015; Stamper and Taylor, 2017; Barkan et al., 2017), although in domains of limited extent. The slow diffusion of salinity limits the simulation domain for DNS to considerably less than a cubic meter of seawater (e.g., Penney and Stastna, 2016).

Alongside the costs of extra grid points to increase resolution, refining the grid also requires a change in the time step of the model. In forward, explicit models the maximum stable time step is governed by the Courant-Friedrichs-Levy (CFL) condition. In words, this condition states that the time step must be shorter than the time it takes for the fastest propagating signal in the model to cross one grid cell. Unfortunately, in common numerical implementations the smallest grid cell and/or the fastest propagating signal set the limit for the whole domain. Implicit scheme models can take larger steps stably, but are generally more expensive per time step and accuracy decreases with step size.

To read the CFL and tera-grid requirements off of Fig. 2.2, choose a length scale for the grid and then follow downward to the fastest allowed timescale (e.g., the sound wave dispersion curve). Count upward the number of orders of magnitude needed to reach the timescale of interest. Subtract that count from 12, and that will be the power of ten available to distribute as grid points at that scale that can delineate the domain.[2] The challenge is quickly apparent. For example, by this method only about 100 spatial grid points are available to study ellipticity in the Pacific if sound waves must be resolved!

Thus, on the larger scales of oceanographic interest, approximations to the equations and parameterizations are used to make a tera-grid more valuable. For example, Charney et al. (1950) approximated their equations so that the fastest propagating signal was the barotropic Rossby wave (shown in red in Fig. 2.2), increasing the time step by many orders of magnitude–particularly so in the oceanic mesoscale between 1×10^4 m and 1×10^5 m. At smaller scales, this *quasigeostrophic* theory (i.e., the motions are nearly horizontal, hydrostatic, and geostrophic) breaks down as ageostrophic effects become important at the submesoscale (Boccaletti et al., 2007; Thomas et al., 2008) and vertical flows become important for deep convection (Julien et al., 2006). The next sections in this chapter describe some of these approximations and the assumptions on which they rely. The final section provides some example parameterizations of smaller, unresolved, scales of motion.

Reduced to fit known equations: Direct Numerical Simulations

Directly resolving all scales of fluid motion is called *Direct Numerical Simulation* (DNS). A useful notion in assessing when the fluid scales are resolved is the idea that small parcels of fluid are in local thermodynamic equilibrium so they can be considered to have uniform thermodynamic properties (p, T, S). These properties would remain unchanged if each parcel were isolated, an idea consistent with molecular diffusion acting to homogenize thermodynamic properties on small scales. The dissipation scales (Kolmogorov, 1941; Obukhov, 1949; Corrsin, 1951) are effective estimates of parcel size. It is not the case that the whole ocean is in thermodynamic equilibrium, which would require it to have uniform temperature and salinity everywhere (Fermi, 1956). For seawater, the scale of a thermodynamic equilibrium parcel tends to be smaller than the Kolmogorov viscous dissipation scale over which energy or velocity is homogeneous.

The state variables that describe each fluid parcel, along with square brackets to denote their SI units, are mass density ($[\rho]$ = kg/m^3), three-dimensional velocity ($[\mathbf{u}]$ = m/s), *in situ* temperature ($[T]$ = K), pressure ($[p]$ = Pa = N/m^2 = kg/m s^2), and mass fraction salinity (mass fractions are

[2] Don't forget you may need a 3D grid!

dimensionless, so $[S] = 1$).[3] The partial enthalpies of salt and freshwater (h_s and h_w) are thermodynamic variables that differ by fluid and solute. The strain rate is $D_{ij} = 1\ (\partial_i u_j + \partial_j u_i)$.[4]

Following Müller (2006), a convenient form for the fundamental equations of motion for seawater in a rotating frame of reference are:

$$\frac{D\rho}{Dt} = -\rho \underbrace{\nabla \cdot \mathbf{u}}_{\text{divergence}}, \tag{1}$$

$$\rho \frac{D\mathbf{u}}{Dt} = \nabla \cdot \underbrace{\left(-p\mathbf{I} + \sigma^{\text{mol}}\right)}_{\text{stress tensor}} - \underbrace{2\rho\boldsymbol{\Omega} \times \mathbf{u}}_{\text{Coriolis}} - \underbrace{\rho\nabla(\phi)}_{\text{geopotential}}, \tag{2}$$

$$\begin{aligned} \frac{DT}{Dt} &= \underbrace{\left(\frac{\partial T}{\partial p}\right)_{\eta,S} \frac{Dp}{Dt}}_{\text{compress}} + \frac{1}{\rho c_p}\left[-\nabla \cdot \underbrace{\left(\mathbf{q}^{mol} + \mathbf{q}^{rad}\right)}_{\text{heat flux}} + \underbrace{D_{ij}\sigma_{ij}^{mol}}_{\text{friction heat}} - \underbrace{\mathbf{I}_S^{mol} \cdot \nabla(h_s - h_w)}_{\text{mixing heat}}\right], \\ &= \underbrace{\left(\frac{\partial T}{\partial p}\right)_{\eta,S} \frac{Dp}{Dt}}_{\text{compress}} - \frac{\nabla \cdot q^{all}}{\rho c_p} + \frac{\dot{q}}{\rho c_p}, \end{aligned} \tag{3}$$

$$\frac{DS}{Dt} = -\frac{1}{\rho}\nabla \cdot \underbrace{\mathbf{I}_S^{mol}}_{\text{salt flux}}, \tag{4}$$

$$\rho = \underbrace{\rho(p, T, S)}_{\text{eqtn. of state}}. \tag{5}$$

The molecular stress, flux, and heating terms indicate the form for the phenomenological flux law approximations which will be discussed more fully below. Standard values of the coefficients–planetary angular rotation rate ($\Omega \approx 7.29211576/\text{s}\hat{\mathbf{k}}$, which is 2π per sidereal day oriented along a vector pointing toward the North Pole and perpendicular to the plane of the celestial equator), specific heat at constant pressure ($c_p \approx 3850$ J/kg K), and thermal expansion coefficient ($\alpha \approx 2.5 \cdot 10^{-4}$/K)–are useful guidelines for simulations and the magnitudes of these terms. Oceanic density varies about 4% with temperature, salinity, and pressure (i.e., depth), but the mean density is 1025 kg/m^3 at the surface. Frequently, constant values of these parameters are used, but if precise estimation of these properties are needed, they can be determined from practical relations to the ocean thermodynamic state (p, T, S). Likewise, the equation of state (5) must be provided to have a closed set with as many equations as unknowns in (1)-(5).

The *geopotential* ($[\phi] = \text{m}^2/\text{s}^2$) contains the gravitational potential (approximately that of a spherical Earth: $\phi_g \approx g_0 r_e^2/r$, $r_e = 6.370 \times 10^6$ m, $g_0 = 9.81$ m/s^2) plus tidal perturbations to the potential plus the centrifugal potential ($\phi_c = (\boldsymbol{\Omega} \times \mathbf{r})\ (\boldsymbol{\Omega} \times \mathbf{r})/2$). The position relative to the center of the Earth is $\mathbf{r}$, and $r = |\mathbf{r}|$. A typical value of the geopotential gradient is $\nabla\phi \approx g_0$, and its orientation

[3] For convenience, salinity is often written in grams per kilogram or in practical salinity units (psu). The psu are a measure of conductivity that is empirically tuned to be nearly the same numerically as grams per kilogram.

[4] Note that Cartesian indices are used on some tensors where needed for clarity. Einstein summation of repeated indices is assumed.

defines the direction we call "vertical" with unit vector **k**, which is not quite the same direction as **r** because the centrifugal force is oriented outward from the Earth's rotation axis as opposed to gravity which is oriented toward the point at Earth's center of mass. In a local Cartesian coordinate system tangent to the ocean surface (which is perpendicular to **k**, not **r**), we use z as the vertical coordinate and x, y to be eastward and northward horizontal coordinates.

Other tracers of interest such as nutrients or dissolved gasses, with τ representing mass fraction, can be evolved using an equation similar to that for salinity,

$$\frac{D\tau}{Dt} = C_\tau^{\text{react}} + D_\tau^{\text{mol}}. \tag{6}$$

Here we admit a source term, C_τ^{react}, in addition to diffusion, so that chemical reactions producing ($C_\tau^{\text{react}} > 0$) or reducing ($C_\tau^{\text{react}} < 0$) the tracer in question or radioactive decay ($C_\tau^{\text{react}} \propto -\tau$) might be represented. The salts that constitute salinity are generally assumed not to react or precipitate, although evaporites, manganese nodules, and other precipitates are found in small quantities.

Forcing at the boundaries is also required. The boundary conditions are, to be evaluated at the position of the surface η,

$$\text{Normal stress: } \underbrace{\mathbf{n}\cdot\left(-p\mathbf{I}+\sigma^{\text{mol}}\right)\cdot\mathbf{n}}_{\text{air, ice, seafloor}} = \underbrace{\mathbf{n}\cdot\left(-p\mathbf{I}+\sigma^{\text{mol}}\right)\cdot\mathbf{n}}_{\text{ocean}} + \underbrace{\gamma\nabla\cdot\mathbf{n}}_{\text{surf. tension}}, \tag{7}$$

$$\text{Tangential stress: } \underbrace{\mathbf{t}\cdot\sigma^{\text{mol}}\cdot\mathbf{n}}_{\text{air, ice, seafloor}} = \underbrace{\mathbf{t}\cdot\sigma^{\text{mol}}\cdot\mathbf{n}}_{\text{ocean}} + \underbrace{\mathbf{t}\cdot\nabla\gamma}_{\text{Marangoni}}, \tag{8}$$

$$\text{Heat: } \underbrace{\mathbf{n}\cdot\mathbf{q}^{all}}_{\text{air, ice, seafloor}} = -\mathbf{n}\cdot\underbrace{\left(\mathbf{q}^{mol}+\mathbf{q}^{rad}\right)}_{\text{ocean}}, \tag{9}$$

$$\text{Kinematic/Freshwater: } \frac{D\eta(x,y)}{Dt} = \mathbf{u}\cdot\mathbf{k} + P - E, \qquad \mathbf{I}_S^{mol}\cdot\mathbf{n} = 0. \tag{10}$$

where **n** and **t** being normal outward from the ocean and arbitrary tangential unit vectors at the surface. The surface tension ($\gamma \approx 0.0728$ N/m) participates in both the normal and tangential stress balances, but the latter depends only on the gradient of γ, which depends on S, T, and surfactants (Marangoni, 1865). The location of the sea boundary $\eta\,(x, y)$ can be altered by vertical motions, precipitation (P), or evaporation (E) at the upper surface. At the lower surface, this boundary condition is equivalent to no-normal flow through the boundary ($\mathbf{u}\cdot\mathbf{k} = \mathbf{u}\cdot\nabla\eta$).

Another way to consider the boundary conditions (7)-(10) is as a flow of a conserved property toward the boundary in one continuum (ocean, atmosphere, or seafloor), and then a flow away from the boundary in the other. If the boundary itself is not capable of storing the conserved property, then the flow toward the boundary in each fluid must be equal and opposite. On the other hand, capillary waves are an example of how energy can be stored in the boundary, because their presence increases potential energy stored in surface tension. For example, any downward momentum flux in the atmosphere must cause a downward momentum flux in the ocean–minus any momentum absorbed by the boundary–which is the essence of (7). Energy, momentum, and mass of freshwater and salt all obey a similar rule. If the boundary does not resist the flow through it, then chemical potentials must be constant across the boundary as well for equilibrium to occur, which sets the humidity and partial pressures of gasses. This thought process is a bit less scale- oriented than (7)-(10), and it can be adapted to account for mushy layers including bubbles, spray, etc., more easily.

Heat and freshwater fluxes also arrive at the ocean surface. In practice, the simulation of evaporation and precipitation fluxes, including bubbles, spray, and droplets, is rather complicated in DNS (Schlottke and Weigand, 2008). The heat exchange equations above, while somewhat idealized, are sufficient for our purposes. The heat fluxes through the ocean surface may be in the form of sensible atmospheric heating ($\approx$ 7 W/m^2), latent heat of evaporation ($\approx$ 100 W/m^2), energy that arrives through condensation or rainfall, and electromagnetic radiation at a variety of wavelengths. Positive numbers indicate ocean cooling by convention here. The shortwave radiation that arrives at the ocean surface is primarily solar ($\approx$ -170 W/m^2), while longwave (infrared) radiation is exchanged back and forth between the ocean and atmosphere, with almost no net exchange but regional and temporal variability of order 10 W/m^2. Shortwave radiation penetrates seawater but decays exponentially with depth through absorption of its energy into seawater. Typical e-folding depths for visible light in seawater are 1 – 100 m depending on wavelength (blues & greens penetrate more deeply) and water clarity. Longwave radiation is absorbed and emitted by only the surface $\approx$ 1 cm. Daily maximum fluxes can be much larger, with solar and latent heat fluxes near 1000 W/m^2 in magnitude. Useful conversions are that 1 mm of evaporation takes an hour with –635 W/m^2 of ocean heating, while freezing 1 mm of water per hour releases 95 W/m^2. The flux values here are taken from the global means estimated by Grist and Josey (2003) and variability is from Bates et al. (2012).

Note that the details of the air-sea interface, including bubbles, spray, and conversions between molecular and turbulent sensible fluxes complicate these exchanges! Reflection of light at the ocean surface, evaporation, and conversions between different forms of energy make it exceptionally hard to be sure about which fluxes balance which. For this reason, often ocean models are forced with a net energy flux at the surface, or a simple breakdown into net surface fluxes and net penetrative (i.e., radiation) fluxes.

Onsager relations

Lars Onsager, while a junior faculty member at Brown, discovered some amazing relationships that help to better understand what thermodynamical equilibrium and diffusion mean in fluid systems (Onsager, 1931a,b). Unfortunately, this work did not overcome his difficulties as a teacher, and he was asked to leave the faculty soon after publication.[5]

The Onsager relations provide functions for the molecular fluxes in (1)-(5) in terms of the gradients (or “forces” in Onsager’s description) of the local thermodynamic properties. What makes the work interesting is that it relates the assumption of local thermodynamic equilibrium to what will eventually occur under global thermodynamic equilibrium if the fluid is left alone. If the fluid is isotropic and locally homogeneous (i.e., in local thermodynamic and dynamic balance), then the relations are

[5] He did win the 1968 Nobel Prize in Chemistry for this work as a consolation.

$$\mathbf{q}^{mol} = a\nabla\left(\frac{1}{T}\right) - b\frac{1}{T}\nabla\left(\mu_s - \mu_w\right)_T, \tag{11}$$

$$\mathbf{I}_s^{mol} = b\nabla\left(\frac{1}{T}\right) - c\frac{1}{T}\nabla\left(\mu_s - \mu_w\right)_T, \tag{12}$$

$$\sigma_{ij}^{mol} = 2\mu D_{ij} - \frac{2}{3}\upsilon D_{kk}\delta_{ij}. \tag{13}$$

The coefficients a, b, c, μ, υ need to be determined for the material under consideration, e.g., the subscripts s and w on μ indicate the Gibbs energy per unit mass of salt or pure water at a given temperature and pressure, respectively. Thus, their difference indicates the change in energy as mass is exchanged between salt and freshwater. Combining these relationships with (1)-(5), it becomes clear that a fluid will not be in equilibrium until: 1) *in situ* temperature is constant, 2) $\mu_s = \mu_w$, and 3) the fluid is strain free, or $D_{ij} = 0$, which is resting or in solid-body motion. For seawater, dynamic viscosities range from $\mu = \upsilon \approx 1.1 \times 10^{-3}$ Pa s for ocean surface conditions and 1.9×10^{-3} Pa s at near freezing temperatures. Taking advantage of the derivatives of the thermodynamic properties and the fact that these diffusivities depend on molecules being present and therefore must be proportional to density, we can express the heat and salt flux in more familiar terms.

$$\mathbf{q}^{mol} = -\rho\left(\kappa_T\nabla T - \kappa_{TS}\left[\nabla S - \gamma\nabla p\right]\right), \tag{14}$$

$$\mathbf{I}_s^{mol} = -\rho\left(\kappa_S\left[\nabla S - \gamma\nabla p\right] + \kappa_{ST}\nabla T\right). \tag{15}$$

$$\kappa_T \equiv \frac{a}{\rho T^2}, \quad \kappa_S \equiv \frac{c}{\rho T}\frac{\partial\left(\mu_s - \mu_w\right)_T}{\partial S},$$

$$\kappa_{TS} \equiv \frac{b}{\rho T}\frac{\partial\left(\mu_s - \mu_w\right)_T}{\partial S}, \quad \kappa_{ST} \equiv \frac{b}{\rho T^2}, \quad \gamma \equiv \frac{\partial\left(\mu_s - \mu_w\right)_T/\partial p}{\partial\left(\mu_s - \mu_w\right)_T/\partial S}.$$

Thus, the molecular fluxes of heat and salt are proportional to the gradients of temperature, salinity, and pressure (albeit with diffusivities that depend on these same properties). Typical values are $\kappa_T = 1 \times 10^{-7}$ m^2/s and $\kappa_S = 1 \times 10^{-9}$ m^2/s. The mixed κ_{TS} and κ_{ST} are less familiar, but are to be expected because the chemical potentials depend on temperature, pressure, and salinity. They are generally negligible in the oceanic case, i.e., if salinity and temperature both vary in such a way as to have comparable magnitude of effect on seawater density (Caldwell and Eide, 1981).

The implications of constant *in situ* temperature and salinity are likewise rarely considered in the ocean, perhaps because of how long it would take for this system to come into equilibrium. The kinematic viscosity of water is about $\mu/\rho_0 = 1 \times 10^{-3}$ Pa s/1025 kg/m^3 = 1×10^{-6} m^2/s. For a 4 km deep ocean, it would take roughly 500,000 years of spin-down after forcing for this viscosity alone to silence the flows in the ocean. The thermal diffusivity is 7 to 14 times slower than viscosity, and salinity and carbon dioxide diffusivity are about 100 times slower than temperature, so diffusive ocean equilibration is a 5-500 million year process. Since we know that the forcing of the ocean varies dramatically on diurnal, synoptic, tidal, seasonal, Milankovitch, and tectonic timescales–all of which are faster than these equilibration timescales: the ocean has never been in global thermodynamic equilibrium.

Heat and temperature

Equations (1)-(5) together with appropriate boundary conditions (7)-(10) and molecular bulk formulae (14)-(15) are a closed set of 7 equations in 7 unknowns (ρ, p, T, S and three components of $\mathbf{u}$). However, they are rarely numerically integrated in this form.

Common oceanographic simplifications remove the compression term on the right side of (3) by choosing a different temperature-like variable instead of *in situ* temperature. One might call (3) the "temperature equation" since it has DT/Dt on the left side, but note that it also has the compression term proportional to Dp/Dt on the right hand side. This equation is actually a recast form of the first law of thermodynamics (work done equals energy change) for a parcel of fluid, which relates changes in energy to external energy fluxes and adiabatic expansion (work done).

The traditional recasting of this equation is in terms of the potential temperature θ, which is defined as the temperature that a fluid parcel would take if relocated to a reference pressure adiabatically, isentropically, and without changing salinity. As we just noted, the molecular viscosity and diffusivity of seawater are quite slow, so it is reasonable to consider such reversible displacements.

A more accurate temperature-like variable is the conservative temperature, Θ, which is part of the TEOS-10 (McDougall and Barker, 2011) framework. This framework is a considerable improvement over the potential temperature and conductivity empirical relations, because it is based on a thermodynamic potential approach using the Gibb's function which provides consistently accurate relationships between all thermodynamically important quantities. The Gibb's function is $\mu_w(1 - S) + \mu_s S$, that is, the salinity-weighted sum of the chemical potential of salt in seawater and freshwater in seawater. These chemical potentials are not constants, but are functions of pressure, temperature, and salinity.

The conservative temperature is proportional (with coefficient C_p^0 for convenience) to the potential specific enthalpy. Akin to the potential temperature, the potential specific enthalpy is the specific enthalpy a parcel would have if relocated to a reference pressure (usually the surface). Propagating these definitions through (3) yields (McDougall, 2003),

$$\frac{D\Theta}{Dt} = \frac{\alpha}{\tilde{\alpha}} \frac{\dot{q} - \nabla \cdot \mathbf{q}^{all}}{\rho C_p^0} - \left(\frac{\alpha}{\tilde{\alpha}} [\mu_s(p) - \mu_w(p)] - [\mu_s(p_r) - \mu_w(p_r)]\right) \frac{1}{\rho C_p^0} \nabla \cdot \mathbf{I}_S^{mol}, \tag{16}$$
$$\Theta(p, \eta, S; p_0) = h(p_0, \eta, S)/C_p^0, \qquad C_p^0 \equiv 3989.24495292815 \mathrm{J/kgK}.$$

While very similar to the potential temperature formulation, in practice (16) is considerably more accurate. It is much easier to implement than (3), because the material derivative for pressure is eliminated so that pressure becomes a diagnostic variable. The coefficients ($\alpha/\tilde{\alpha}$, C_p^0) vary extremely little, as C_p^0 is a constant by definition and $\alpha/\tilde{\alpha} \approx 1$ to within 0.2%. For the same reason, when energy exchanges at the surface are used to alter the conservative temperature, assuming $\alpha/\tilde{\alpha} \approx 1$, the resulting heat uptake is accurate. Finally, specific enthalpy $h = e_i + p/\rho$ is closely related to the specific internal energy e_i, but unlike energy, entropy, or potential temperature, it is particularly easy to model because it is mixed simply by mass proportion (like salinity or mass) when two water parcels are combined at uniform pressure (although mixing also changes the entropy, which affects this simple rule). While potential specific enthalpy (and therefore conservative temperature) is only approximately mixed by mass proportion, it is much closer to being so than temperature, potential temperature, entropy, etc.

Reduced by approximate dynamics: Sound waves and the Boussinesq approximation

Our detailed equations of motion for seawater, including the local thermodynamic properties can be written as

$$\frac{D\rho}{Dt} = -\rho\nabla\cdot\mathbf{u}, \tag{17}$$

$$\frac{D\mathbf{u}}{Dt} = \frac{1}{\rho}\nabla\cdot\left(-p\mathbf{I}+\sigma^{\mathrm{mol}}\right) - 2\mathbf{\Omega}\times\mathbf{u} - g\mathbf{k}, \tag{18}$$

$$\frac{D\Theta}{Dt} \approx \frac{\dot{q}-\nabla\cdot\mathbf{q}^{all}}{\rho C_p^0} \tag{19}$$

$$\frac{DS}{Dt} = -\frac{1}{\rho}\nabla\cdot\mathbf{I}_S^{mol}, \tag{20}$$

$$\rho = \rho(p,\Theta,S). \tag{21}$$

The molecular effects are given by (11)-(13) and the boundary conditions are given by (7)-(10). However, these equations are slow to compute solutions for, as the sound speed limits the possible time step. In this section, we'll explore how sound waves arise and what can be done to ameliorate this issue.

For reversible motions (i.e., those where entropy and salinity are constant), we can convert between the rate of change of density and pressure.

$$\left(\frac{Dp}{Dt}\right)_{S,\eta} = \left(\frac{\partial\rho}{\partial p}\right)_{S,\eta}\left(\frac{D\rho}{Dt}\right)_{S,\eta} = c^2\left(\frac{D\rho}{Dt}\right)_{S,\eta}. \tag{22}$$

The proportionality constant is the sound speed ($c \approx 1484$m/s) squared, which is a function of the ocean thermodynamic state (p, T, S). If we allow some irreversible processes to occur, they can be absorbed into a diffusion of pressure in a rewritten form of (1).

$$\frac{Dp}{Dt} = -\rho c^2\nabla\cdot\mathbf{u} + D_p^{\mathrm{mol}}. \tag{23}$$

If this equation and (18) are linearized into small perturbations (indicated by primes, neglected when multiplied together) about a homogenous, stationary background state at rest (indicated by bars, with density and sound speed taken as a constant), they can be combined to eliminate ρ and $\mathbf{u}$.

$$p = p' + \overline{p}, \rho = \rho' + \overline{\rho}, \mathbf{u} = \cancelto{\mathrm{U}}{\overline{\mathbf{u}}} + \mathbf{u}', \rho\mathbf{u} = \overline{\rho}\mathbf{u}' + \rho'\mathbf{u}' \approx \overline{\rho}\mathbf{u}', \tag{24}$$

$$\frac{\partial p'}{\partial t} = -\overline{\rho}c^2\nabla\cdot\mathbf{u}' + D_p^{\mathrm{mol}}, \qquad -\nabla\overline{p} = \nabla\phi, \tag{25}$$

$$\overline{\rho}\frac{\partial\nabla\cdot\mathbf{u}'}{\partial t} = -\nabla^2 p' - 2\overline{\rho}\nabla\cdot\mathbf{\Omega}\times\mathbf{u}' + \nabla\cdot\sigma^{\mathrm{mol}\prime}, \tag{26}$$

$$\frac{\partial p'}{\partial t} + c^2\nabla^2 p' = -2c^2\overline{\rho}\boldsymbol{\Omega}\cdot\nabla\times\mathbf{u}' - c^2\nabla\cdot\sigma^{\mathrm{mol}\prime} + D_p^{\mathrm{mol}}. \tag{27}$$

The last equation is the sound wave equation. This equation presents difficulties for numerical modeling, because of the CFL limit for such fast waves (time steps of a few milliseconds for typical grids!). Implicit numerical schemes can be used to remove these waves, but a more common approach is to use a set of reduced equations that emphasize phenomena that travel slower than the speed of sound. This can be accomplished through a number of reduced systems (e.g., the anelastic equations), but the most common oceanographic set relies on the Boussinesq approximation.

Equation (23) connects the change in pressure and density that comes with compression of seawater. But, as seawater is a liquid and not a gas, we know that it is highly resistant to compression. Indeed, even over the immense pressure differences between the surface and the abyss, seawater density changes by only a few percent. So, let us consider a background value of density, a horizontally-averaged density contribution that changes only in the vertical to represent stratification, and a density variation in space and time. For convenience, we write these in terms of buoyancy, which is just minus the density perturbations rescaled to have units of gravitational acceleration.

$$\rho = \rho_0\left(1 + \overline{b}(z)/g + b(x,y,z,t)/g\right). \tag{28}$$

If we assume that density is nearly its background value, i.e., $b(x, y, z, t)$ and $\overline{b}(z)$ are much smaller than g, and neglect all higher order contributions, then our equations become

$$0 \approx \nabla\cdot\mathbf{u}, \tag{29}$$

$$\frac{D\mathbf{u}}{Dt} = \frac{1}{\rho_0}\nabla\cdot\left(-\phi\mathbf{I} + \sigma^{\mathrm{mol}}\right) - 2\boldsymbol{\Omega}\times\mathbf{u} + b\mathbf{k}, \tag{30}$$

$$\frac{D\Theta}{Dt} \approx \frac{1}{\rho_0 C_p^0}\left[-\nabla\cdot\left(\mathbf{q}^{mol} + \mathbf{q}^{rad}\right) + D_{ij}\sigma_{ij}^{mol} - \mathbf{I}_S^{mol}\cdot\nabla(h_s - h_w)\right] \tag{31}$$

$$\frac{DS}{Dt} = -\frac{1}{\rho_0}\nabla\cdot\mathbf{I}_S^{mol}, \tag{32}$$

$$b = b(z,\Theta,S). \tag{33}$$

Buoyancy appears only in the gravitational term, and only the spatially variable buoyancy at that, because only it can contribute to horizontal gradients of dynamic pressure ϕ, unlike the ρ_0 and $\bar{\rho}$ which contribute only to the background hydrostatic pressure which is constant in the horizontal. These background fields are related to one another by

$$\frac{\partial}{\partial z}(p-\phi) = -\rho_0(g+\overline{b}), \qquad N^2 = \frac{\partial\overline{b}}{\partial z}. \tag{34}$$

The equation of state (33) depends on depth, not pressure, unlike (21). There are a few reasons for this choice. First, calculating the total thermodynamic pressure is a bit awkward in the Boussinesq system. Second, in a nearly incompressible fluid depth and background pressure are monotonically related and thus interchangeable. Finally, Vallis (2006) notes that this choice makes defining energy in the Boussinesq equations more consistent.

In general, care is needed with energetics as Boussinesq models have no conversion of internal energy to mechanical energy, but do allow conversion between potential and kinetic energy via sinking of dense water or rising of light water via vertical velocity times buoyancy: *wb* (Young, 2010). In a stably-stratified ocean, *wb* keeps water parcels near a fixed location. The restoring force for internal waves (where $wb < 0$) is a good example. A second important role for *wb* is as the source of energy for baroclinic instabilities, which convert mean potential energy to eddy energy by correlating eddy motions with water buoyancy (thus $wb > 0$ on average). Likewise, unstable density profiles convect with $wb > 0$. Also, the care required to handle the compressible aspects resulting in conservative temperature are not lost! Equation (31) is significantly different than (3) in terms of the stratification it predicts in (34), which in turn sets the level of stratification felt by the flow.

These equations behave differently from the compressible set. The sound waves above required a three-dimensional divergence in velocity. In these Boussinesq (1897) approximation equations, the velocity field does not diverge, so sound waves are eliminated as desired. Furthermore, the subtle distinctions between properties per unit mass and properties per unit volume are lost–those conversions now all occur with the background density ρ_0. Finally, the equation that plays the role of conservation of mass (29) doesn't even feature the units of mass! Now, the volume of fluid is conserved. Because the density is still allowed to vary somewhat (through the buoyancy), actual mass is no longer conserved. This fact means that the calculation of subtle mass budgets, e.g., those required to calculate sea level rise, require careful thought (Griffies and Greatbatch, 2012).

Dimensionless equations and scales

The Boussinesq equations (29)-(33) are an efficient alternative to the compressible equations (17)-(21) when we are not interested in sound waves. Perhaps there are other simplifications we can arrive at by neglecting other terms in these equations. The general technique for exploring the size of different terms in the equations is scale analysis, which is most natural in a dimensionless form of the equations of motion. In dimensionless equations, the expected size of each term is made explicit so small terms that may be neglected are highlighted. Taking the Boussinesq equations (29)-(33) in a rotating frame, and simplifying friction terms, we arrive at a set of equations convenient for dimensional analysis (following Lilly, 1983; McWilliams, 1985; Bachman et al., 2017a). One simplifying assumption in addition to the preceding equations is that we now assume that the rotation axis, and hence **f**, is aligned with the local vertical **k**, which is sometimes called the *traditional approximation*.

Next, we choose the approximate scales of the dimensional variables. The 3D velocity in the Boussinesq equations (29)-(33) (**u**) is partitioned into the horizontal velocity ($\mathbf{v}_h$ with typical scale V_*) and vertical velocity (w) based on gridscale parameters of vertical grid scale (Δz) and horizontal grid scale (Δs). A locally-linear equation of state[6] will be assumed, so that $\bar{b}(z) + b(x, y, z, t) = \bar{b} + \mathrm{b} = g(\alpha[\bar{\theta} + \theta] - \beta[\bar{S} + S])$. Scalings for perturbation pressure ($\phi \sim \phi_0 = \max(V_* f_0 \Delta s, V_*^2)$),

[6] That is, α, β may vary but their gradients will be neglected in favor of the larger S, θ variations here.

stratification ($\partial_z\bar{b} \sim N_*^2$, $\partial_z\bar{S} \sim N_*^2/g\alpha$, $\partial_z\bar{\Theta} \sim N_*^2/g\beta$), perturbation active tracers ($b \sim \phi_0/\Delta z$, $\theta \sim \phi_0/\Delta zg\alpha$, $S \sim \phi_0/\Delta zg\beta$), and vertical velocity ($w \sim \phi_0 V_*/N^2\Delta z\Delta s$) are used.

Taking these dimensional scalings for all of the variables, we can construct a set of equations for all of the dimensionless variables. A dimensionless variable is just the dimensional one divided by its scale, e.g., the dimensionless horizontal velocity is just the dimensional horizontal velocity divided by V_*. After substituting in all of these scale factors into (29)-(33), they are collected into dimensionless factors which will be named and then interpreted below. The equations for the dimensionless variables are:

$$\mathrm{Ro}_*\left[\partial_t\mathbf{v}_h + \mathbf{v}_h\cdot\nabla\mathbf{v}_h + \epsilon w\partial_z\mathbf{v}_h\right] + \underbrace{\left(1+\frac{y\mathrm{Pl}_*}{\Delta y}\right)\mathbf{z}\times\mathbf{v}_h + \mathrm{M}_{R_*}\nabla_h\phi}_{\text{geostrophic}} = \frac{\mathrm{Ro}_*}{\mathrm{Re}_*}\nabla_i\sigma_{ih}, \tag{35}$$

$$\mathrm{Fr}_*{}^2\frac{\Delta z^2}{\Delta s^2}\left[\partial_t w + \mathbf{v}_h\cdot\nabla w + \epsilon w\partial_z\mathbf{v}_h\right] + \underbrace{\partial_z\phi - b}_{\text{hydrostatic}} = \frac{\mathrm{Fr}_*{}^2\Delta z^2}{\mathrm{Re}_*\Delta s^2}\nabla_i\sigma_{iz}, \tag{36}$$

$$\partial_t S + \mathbf{v}_h\cdot\nabla S + \epsilon w\partial_z S + w\partial_z\bar{S} = \frac{1}{\mathrm{Pe}_*}\nabla\cdot\mathbf{I}_S^{all}, \tag{37}$$

$$\partial_t\Theta + \mathbf{v}_h\cdot\nabla\Theta + \epsilon w\partial_z\Theta + w\partial_z\bar{\Theta} = \frac{1}{\mathrm{Pe}_*}\nabla\cdot\mathbf{I}_\theta^{all}, \tag{38}$$

$$\partial_t b + \mathbf{v}_h\cdot\nabla b + \epsilon w\partial_z b + w\partial_z\bar{b} = \frac{1}{\mathrm{Pe}_*}\nabla\cdot\left(\alpha\mathbf{I}_\theta^{all} - \beta\mathbf{I}_S^{all}\right), \tag{39}$$

$$\nabla\cdot\mathbf{v}_h + \epsilon\partial_z w = 0, \tag{40}$$

$$\mathrm{M}_{R_*} \equiv \max(1,\mathrm{Ro}_*), \qquad \epsilon \equiv \frac{\mathrm{Fr}_*{}^2}{\mathrm{Ro}_*}\mathrm{M}_{R_*} = \begin{cases} \mathrm{Fr}_*{}^2 & \mathrm{Ro}_* \geq 1, \\ \mathrm{Ro}_*\mathrm{Bu}_*{}^{-1} & \mathrm{Ro}_* < 1 \end{cases} \tag{41}$$

When h or z are used as a subscript, only the horizontal components or vertical component of that variable are relevant, respectively. Repeated indices are summed over all three directions. Note that σ_{ih}, σ_{iz} represent projections of an overall (symmetric) stress tensor into horizontal and vertical directions. Only the leading order term involving Pl_* is retained, given its small size on the grid scale of operational models.

Working from the perspective of model development, it is most useful to consider the scaling behavior with lengthscales based on the model grid scale as this set has. Following Fox-Kemper and Menemenlis (2008), an asterisk denotes resolved model fields, as opposed to the abstract field variables. The dynamics that should occur at the grid scale are precisely the largest features that the model cannot resolve, and thus the phenomena whose effects that are likely most important to parameterize within our chosen model. These convenient dimensionless parameters are formed using the discretization scales of the grid (horizontal: $\Delta s = \sqrt{\Delta x\Delta y}$, vertical: Δz). We begin by identifying the grid Rossby number ($\mathrm{Ro}_* = U_*/f_0\Delta s$), baroclinic Froude number (see below), and planetary number ($\mathrm{Pl}_* = \Delta y\,\frac{\partial f}{\partial y}/f_0$) as important. $\mathrm{M}_{R*}/\mathrm{Ro}_*$ is the Euler number, and can be taken to be the maximum of 1 and Ro_*^{-1}. Also, the grid aspect ratio ($\delta = \Delta z/\Delta s$), Reynolds number ($\mathrm{Re}_* = U_*\Delta s/\nu_*$), and Péclet number ($\mathrm{Pe}_* = U_*\Delta s/\kappa_*$) are needed to establish how much damping is required. Note that ν_* denotes an "eddy viscosity" which is to be used in a numerical model rather than measured experimentally. Numerical stability requires Re_* and Pe_* to be O(1). Parameterization examples determining viscosity are given in the last section before the conclusions.

The first baroclinic deformation radius L_d is approximated in variable stratification by Chelton et al. (1998) as

$$L_d = \frac{1}{|f|\,\pi}\int_{-H}^{0} N_*(z)\,dz. \tag{42}$$

If the Froude number is defined similarly (LeBlond and Mysak, 1978), then

$$\mathrm{Fr}_* = \frac{V_*}{\int_{-H}^{0} N_*(z)\,dz}. \tag{43}$$

With these definitions the gridscale Burger number (Bu_*) relates the deformation radius to grid scale: $\pi L_d/\Delta s = \mathrm{Ro}_*/\mathrm{Fr}_* = (\mathrm{Bu}_*)^{1/2}$, so a large Burger number implies a well-resolved deformation radius. In order for this to be consistent with the values of N_*^2 used above, the vertical average of N_* should be used as the scale factor.

With either small Froude number (Fr_*) or a grid with shallow aspect ratio ($\Delta x \gg \Delta z$), or both, (36) reduces to the hydrostatic balance. A large Froude number, on the other hand, implies very weak stratification which is likely to allow 3D overturning and large vertical velocities. However, in this case, the overturning plumes may be horizontally small, so a convective parameterization or square or tall aspect ratio grid is needed to capture these effects. Hydrostatic models have a simplified vertical momentum balance, which means that the pressure is simply the weight per unit area of fluid above and the vertical accelerations are small compared to gravity. Hydrostatic models are typically used for most oceanographic applications, because ocean models tend to have shallow aspect ratios and small Froude number. Hydrostatic models are appropriate to study the submesoscale and larger scales. The hydrostatic, Boussinesq equations are sometimes called the *primitive* equations of oceanography.

Similarly, small Rossby number (Ro_*) at the gridscale leads to a dominantly geostrophic balance in (35). The Rossby number compares the Coriolis force to advection and acceleration. Fluids with small Ro_* can be thought of as *rapidly rotating*–that is, the rotation of Earth is fast compared with the rotation and acceleration of the fluid relative to Earth.

The quasigeostrophic equations–the system that results from hydrostatic (small Froude number and shallow aspect ratio) and nearly geostrophic motions (small Rossby number)–remain a popular tool for studying mesoscale dynamics and building subgrid schemes for mesoscale-permitting models (Jansen and Held, 2014; Straub and Nadiga, 2014; Shevchenko and Berloff, 2015; Chen et al., 2016). One reason for their popularity is that inertial, internal gravity, and Kelvin waves are filtered out of explicit treatment in the quasigeostrophic equations, similarly to how sound waves are filtered out by the Boussinesq approximation. As a result, the quasigeostrophic system can take time steps that are orders of magnitude larger than the hydrostatic, Boussinesq equations (Fig. 2.2). Indeed, it was the quasigeostrophic system which Charney discovered during his Ph.D. work and that Charney et al. (1950) used for the first successful weather models. The quasigeostrophic equations have only non-divergent, horizontal, geostrophic motions at leading order, and while this removes the gravity waves formally they cannot be applied globally because of the way the Coriolis parameter is scaled and their inability to handle the equator.

Extremely small Rossby number can make a different approximation appropriate: the planetary geostrophic equations. These equations neglect acceleration and advection of momentum altogether. The only *D/Dt* terms that are retained are those in the salinity, temperature, and thus buoyancy equations. The planetary geostrophic equations can be used globally, and they are very efficient for low-resolution, long-duration simulations. These equations are often used for theory (Luyten et al., 1983; Huang and Flierl, 1987; Fox-Kemper and Ferrari, 2009), but only rarely (Samelson and Vallis, 1997; Olbers and Eden, 2003) are equations in this regime used for numerical modeling.

Characteristic Motions by Scale

It is a start to have an idea of what reduced, closed sets of equations might result at different scales, but there are behaviors that aren't easily described this way. For one, we will want to distinguish motions that are relatively steady (i.e., currents) from waves and turbulence. Also, not every behavior noted in Fig. 2.2 has its own equation set, but still they are all different enough to be named distinctly! Without being too exhaustive, here we will examine some of the most commonly discussed scales and their dominant behaviors.

Currents, waves, and turbulence

Currents

A current is a persistent pattern of velocity that can transport seawater, along with other properties, from place to place. On large scales away from the equator, currents tend to be in geostrophic balance. On small scales currents can be topographically constrained (e.g., river plumes, tidal channels, island wakes, etc.).

Waves

Unlike a current a wave transports information by the propagation of the wave, which may not require moving the seawater along with the wave. Often we think of a wave as a repeating sinusoid or as a crest approaching shore and breaking, and the sinusoidal wave is helpful in understanding the dispersion curves in Fig. 2.2. Mathematical descriptions of waves can be linear or nonlinear, but the waves that are solutions to (35)-(40) neglecting all nonlinear terms are useful to consider. As a simple example, we can neglect the effects of advection altogether by simply linearizing perturbations about a state of rest in (29)-(33). Furthermore, let's simplify by neglecting radiation, friction heating, and mixing heating, and removing the background stratification in Θ and S that is already in balance with diffusion, and note that small deviations away from this background (with primes) will not distinguish between Θ and T, then

$$0 = \nabla \cdot \mathbf{u}', \tag{44}$$

$$\frac{\partial \mathbf{u}'}{\partial t} = \frac{1}{\rho_0}\nabla \cdot \left(-\pi'\mathbf{I} + \sigma^{\mathrm{mol}}\right) - 2\boldsymbol{\Omega} \times \mathbf{u}' + \left(\frac{\partial b}{\partial \Theta}\Theta' + \frac{\partial b}{\partial S}S'\right)\mathbf{k}, \tag{45}$$

$$\frac{\partial \Theta'}{\partial t} + w' \frac{\partial \overline{\Theta}}{\partial z} \approx \frac{1}{C_p^0} \nabla \cdot \left(\kappa_T \nabla \Theta' - \kappa_{TS} \nabla S' \right) \tag{46}$$

$$\frac{\partial S'}{\partial t} + w' \frac{\partial \overline{S}}{\partial z} = \nabla \cdot \left(\kappa_S \nabla S' + \kappa_{ST} \nabla \Theta' \right). \tag{47}$$

This set of linear equations is closed, and every term in all of the equations depends linearly on a perturbation variable. One obvious solution to this set is thus $\mathbf{u}' = 0$, $S' = 0$, $\Theta' = 0$, $b' = 0$.

However, waves are the nonzero free modes of this system, which can occur only if the set of equations is singular. Again, for simplicity consider the case of plane sinusoidal waves, where every partial derivative of a primed quantity is replaced by multiplication by a frequency or a wavenumber (2π divided by the wavelength, which is $2\,\pi$ times the number of wave crests per unit distance). This set of equations then becomes a matrix set like,

$$\mathcal{L}(\omega, k, l, m) \begin{bmatrix} u' \\ v' \\ w' \\ \Theta' \\ S' \\ \pi' \end{bmatrix} = 0. \tag{48}$$

If the matrix $\mathcal{L}$ can be inverted, then the solution is just zero. If it can't be inverted, then the matrix is singular. The characteristic equation of that matrix will be a sixth-order polynomial, which will depend on the background stratification, frequency, and wavenumber. Each root of that equation will be the dispersion relation of a plane wave under the assumptions just described.

Linear, steady plane waves are reversible in time (you can check this by reversing time in the equations and see if you can rewrite them to be identical to the original set), thus they may wobble back and forth or up and down everywhere, but they do not permanently alter the state of the ocean after averaging over a wave period. Thus, currents and linear, steady plane waves do not interact meaningfully. While these waves are beautiful and interesting objects on their own, if you are interested in mapping the currents in a region—averaging over many wave periods—you don't need to consider them. Furthermore, a matrix system like (48) has a family of solutions for each wavenumber and frequency. Linear systems that result from the fluid equations tend to be *orthogonal* and thus the different waves do not interact with one another. Similarly, a linear plane wave with a given frequency and wavenumber tends to preserve those properties unless it enters a region of different stratification or shear (then it is no longer a plane wave!). However, if you reintroduce the nonlinear or damping terms, this is no longer true. Damped or strongly nonlinear (often called *breaking*) waves can and do affect the mean state and currents of the ocean, as well as each other. Energy gets transferred from wave to wave and frequency to frequency. Understanding these wave-wave interactions is an active topic of research (Nazarenko, 2011).

Of course, plane waves are not the whole story, because the ocean has a surface and a bottom, and the stratification in Θ and S may vary in the vertical as well. Shear and stratification also vary horizontally from region to region as well. The set of waves in such a complex domain is an even larger set of phenomena, as the kinematic and pressure boundary conditions must now be brought to bear on variations in sea surface height. These new degrees of freedom bring surface gravity waves and other free modes of the system.

When waves depend on location such as these surface-bound examples, another important effect occurs: the Stokes drift. The Stokes drift is the difference between the average velocity of all waves and currents averaged sitting at one location (Eulerian velocity) and the average velocity following the trajectory of a fluid parcel in those waves and currents (Lagrangian velocity). The Stokes drift allows waves that vary in space to participate in the processes that permanently transport material and water parcels. Thus, waves with Stokes drift can move flotsam, form windrows, and drive turbulence.

Turbulence

Waves are easier to handle when they are linear or weakly nonlinear. Turbulence is the opposite extreme, intermittent flows that are most easily understood in the strongly nonlinear limit. In oceanography usage, "turbulence" covers a wide range of phenomena. What they all have in common is strong nonlinear effects through the advection of momentum, energy, or tracers. Turbulence research began with the study of isotropic, 3D, incompressible, constant density turbulence (Reynolds, 1895; Kolmogorov, 1941). Oceanographers are very concerned as well with temperature and salinity effects and stratification and the effects of the planet's rotation. Thus, the traditional approach needed, and in many important ways still needs, adaptation for relevance to oceanography.

The Onsager relations, and the beautiful form of the resulting diffusivities and stress tensor, relies heavily on the idea that the molecular motion is isotropic and locally homogeneous. Oceanographic turbulence, particularly submesoscale and mesoscale turbulence, is not isotropic and often not homogeneous. If turbulence behaved just as molecules do–resisting the development of gradients in temperature and salinity through isotropic mixing that leads to fluxes oriented down the gradient of these properties, then Onsager's theory could be modestly adapted. Müller (2006) works through this analysis, and provides "eddy" viscosity and diffusivity closures.

However, the vertical direction is special in that it orients the stratification, and the orientation of the rotation axis is also an important broken symmetry. The Taylor-Proudman theorem states that rapidly rotating, unstratified fluids will "stiffen" along the rotation axis and resist shear in the direction of the rotation axis. In contrast, the presence of stratification "lubricates" the flow leading to larger velocities in the horizontal than the vertical. Furthermore, a major ingredient of the molecular theory is that there is a scale separation between the paths of the molecules and the gradients they act on. Turbulence tends to mimic the properties and locations of its energy source, so that eddies shed from the Gulf Stream are strongest near the stream, nearly the same size, flow with similar velocity, and are comprised of similar water types. Thus, no scale separation exists. On the other hand, turbulence within a boundary layer is limited to the scale of the boundary layer, which might be significantly smaller than a large-scale ocean model, which means in this case there is a scale separation.

To manage the modeling when there is sometimes a scale gap and sometimes not, two methods of analysis and parameterization have arisen. The first, Reynolds-averaged theory (Reynolds, 1895), relies on a scale separation between the turbulence and the resolved flow. The key mathematical aspect of this approach is that once averaging of the turbulence up to the gridscale of the model has occurred, averaging again gives the same result. The second approach is Large Eddy Simulation (Smagorinsky, 1963; Deardorff, 1970). This approach expects that the simulation takes place within the middle of a range of turbulent motions. The largest are resolved and the smallest are parameterized. The model grid lies in between. Here the key concept is the idea of simulation of a filtered version of reality. The filter reduces the small scales and doesn't affect the large scales. However, if the filter is applied twice, the effect is different than applying it only once.

One excellent way to begin to quantify turbulence and waves is using a *power spectrum*. The power spectrum breaks up the energy, or temperature variance, or salinity variance, etc. into contributions from different frequencies and/or wavenumbers. Waves will have their energy concentrated along their dispersion relations, which may be peaked near forcing frequencies (e.g., tides or seasons) with the corresponding wavenumbers to match. Turbulence tends instead to have power spectra that obey a power-law distribution. For example, the kinetic energy power spectrum of 3D, isotropic, homogeneous turbulence is nearly proportional to wavenumber to the -5/3 power. This means that energy is not concentrated in only some particular modes of turbulence, but distributed over all of the modes in a special way as a function of scale. This is one of the most powerful notions for the motions of the oceans.

Basin scales

The largest scales of ocean motions reflect the large scale forcing patterns of winds, tides, and thermal forcing. Two key concepts are the Ekman (1905) and Sverdrup (1947) balances. These balances of Coriolis force and winds form constraints on the currents that are consistent with large-scale steady wind patterns.

The Ekman transport is the mass transported directly by the wind, and this transport can converge and diverge. Ekman effects are particularly profound near coasts and the equator. These convergences and divergences set up patterns in vorticity and pressure that are the key drivers of the gyres and the Antarctic Circumpolar Current (ACC), so these phenomena are indirectly driven by the wind. The Ekman transport also participates importantly in the MOC–forcing the surface branches of the subtropical cells and the Southern Ocean overturning. The Ekman transport is a balance involving the Coriolis force, so it is only achieved after Earth has rotated a few times–it is a subinertial motion. Transient winds that are more rapid than the inertial period tend to drive near-inertial oscillations and gravity waves. Overall, atmospheric forcing on large scales drive transient ocean responses that tend to be more responsive as the frequency of the forcing gets slower (Hasselmann, 1976).

Above, a contrast was made between the gyres–with their horizontal circulations and vertical vorticity– and the cells of the MOC–with their overturning circulations and zonal axis of vorticity. Outside of the regions where they concentrate into boundary currents, the gyres are a result of Ekman and Sverdrup balances (or similar theories that may include bottom slope as well, Wunsch and Roemmich, 1985). The planetary geostrophic equations can be used together with the Ekman transport to simulate the gyres outside of boundary currents. These scales have mostly horizontal motions with only small divergences due to deepening layers and the latitudinal variations of the Coriolis parameter. Thus, the vertical vorticity exceeds the divergence. Depending on basin, the gyres have different mass transport (here expressed with vertically-integrated volume streamfunction Ψ, which is related to the vertical vorticity by a Laplacian derivative), basin width L_b, and depth H, but a rough estimate can be made for the vertical relative vorticity nonetheless:

$$\zeta_z = \nabla^2 \frac{\Psi_z}{H} \approx \frac{\Psi}{L_b^2 H} = \frac{50\mathrm{Sv}}{L_b^2 H} \approx 5 \times 10^{-6}\, \mathrm{f}. \tag{49}$$

The vorticity is compared to f, so that the coefficient can be interpreted as a (very small) Rossby number, $\mathrm{Ro}_* \approx 5 \times 10^{-6}$. The typical Froude number of a gyre interior is also quite small ($O(2 \times 10^{-4})$), given the velocity scales from Ekman and Sverdrup balances of only O (1 cm s^{-1}).

The MOC has important forcing from wind and tidal mixing (Munk and Wunsch, 1998), but increasingly has become understood as a blend of wind-driven overturning, cooling, and mixing (Gnanadesikan, 1999). A key method by which the MOC has been measured is through tracking watermasses as they interleave between one another (Talley, 2008). One interesting question is whether the spread of these watermasses is best understood as a current or as a diffusive or other kind of turbulent dispersion (Lozier, 2010). It is important to recognize that while the MOC and gyres can be distinguished in effect using different vorticity components, their forcing mechanisms are deeply and intricately linked (Yeager, 2015). The horizontal vorticity of the MOC is larger than the relative vorticity of the gyres,

$$\zeta_x = \nabla^2 \frac{\Psi_x}{L_b} \approx \frac{\Psi}{L_b H^2} = \frac{50\mathrm{Sv}}{L_b H^2} \approx 0.05\, \mathrm{f}. \tag{50}$$

However, most of this overturning is very shallow, and the deeper circulations of NADW and AABW are very slow as they spread through the deep oceans, taking hundreds to thousands of years to refresh the abyss (Gebbie and Huybers, 2012). These slow currents lead to a small Froude number, despite the relatively low stratification below the pycnocline.

Another basin scale feature is the ACC. It is the ocean current most like an atmospheric circulation, as it is not bounded by continents and so it flows around the Earth relatively unimpeded. Dynamically, the winds and surface Ekman transport away from Antartica provide this current with potential energy and momentum. The many smaller eddies and fronts that form within the current play an important role in balancing these budgets (Johnson and Bryden, 1989; Radko and Marshall, 2006). The Ferrel cell is the atmospheric circulation most like the Deacon cell, which is the MOC associated with the ACC, because the mean flow in both cells work to strengthen thermal gradients, but eddies and storms work to overturn in the other direction and dominate the heat transport overall.

There are a number of basin scale modes of variability. Perhaps the most famous is El Nino, which is a coupled oscillation of the ocean and atmosphere. The Pacific Decadal Oscillation resembles El Nino but is slower, and variability of the Atlantic and Indian Oceans' equatorial regions have variability that is similar dynamically to El Nino as well. However, there are other basin-scale oscillating modes of the ocean that are not coupled between the atmosphere and ocean: Rossby basin modes. These large-scale modes are basin-filling Rossby-Kelvin waves that may be excited by long tides, seasons, or other low-frequency climate modes. While these waves are basin-wide, as Rossby waves are fastest when they are large, these modes can be surprisingly fast, especially for the barotropic modes (basin transit time on O(weeks)). Decadal variability in sea surface temperature, sea surface height, and regional climate generally may have predictability due to baroclinic Rossby modes and related phenomena (Meehl et al., 2014).

Based on the idea of a critical Reynolds number, beyond which all motions will be turbulent, and the enormous Reynolds number of basin scale motions ($Re \approx 1 \times 10^{11}$), one might expect that the motions on the basin scale might directly stimulate a cascade of turbulence directly, filling in a power law from the largest scales all the way down to the Kolmogorov scale. However, the effects of rotation and stratification prevent this from occurring. With small Ro_*, Fr_* and $\in$ the nonlinear terms in the momentum equations critical to turbulence are emasculated by the hulking Coriolis and stratification terms. The huge potential energy on these large scales vastly exceeds their kinetic energy, as the geostrophic flows enclose stores of potential energy and there are few instabilities or turbulent features capable of accessing it. Only on the mesoscales will turbulence arise.

Mesoscales

At the mesoscale a few different effects combine to make this range of scales the largest scale where ocean turbulence (of the rotating, stratified kind) is found. Because these eddies are the largest and most energetic turbulent eddies in the ocean (Fig. 2.3), they tend to have the largest horizontal turbulent transport of properties. Thus, from the modeling perspective, if these scales are not resolved they must be parameterized, and if they are resolved care is needed to handle them (ensembles, numerics, and scale-aware parameterizations schemes to avoid double-counting the resolved features).

The equations governing the gyres and MOC are actually not capable of closing these circulations at only the basin scale. Western boundary currents (Stommel, 1948; Munk, 1950; Charney, 1955) are *required* to close the Ekman and Sverdrup circulations without a basin-filling inertial circulation (Fofonoff, 1954; Veronis, 1966; Fox-Kemper and Pedlosky, 2004). The MOC, too, has deep western boundary currents for similar dynamical reasons (Stommel and Arons, 1960). Wherever Ekman transport is directed away from the coast, upwelling (or eastern[7]) boundary currents form. These boundary currents focus the large scale kinetic and potential energy into mesoscale-sized intense currents.

So, just how big is the mesoscale? It is deformation radius-sized. The deformation radius compares the scale of the Coriolis parameter to the stratification and width to depth. When the width is just right (the deformation radius), the Coriolis effect is the same size as the stratification effect. Another way to understand the deformation radius is that it is the scale where kinetic and potential energy in a geostrophic current are the same magnitude. Very loosely, the mesoscale can be considered to be in the 10 to 300 km range, but it is considerably more accurate to relate the

[7] Although they need not necessarily be on the eastern side of oceans.

mesoscale to motions near the first baroclinic deformation radius which varies globally and with stratification.

We can follow the same rough vorticity scaling to estimate the vorticity in a boundary current of width L_f, and hence its Rossby number,

$$\zeta_z = \nabla^2 \frac{\Psi_z}{H} \approx \frac{\Psi}{L_f^2 H} = \frac{50\mathrm{Sv}}{L_f^2 H} \approx 0.05\,\mathrm{f}. \tag{51}$$

So, Ro ≈ 0.05. Similarly, we can estimate the Froude number for such a current (≈ 1 m s^{-1}) to be $\mathrm{Fr}_* \approx 0.1$ with a typical value of N ≈ 0.01 cycles/s. Now, with the same scales, the deformation radius is ($L_d \approx 30$ km) and $\epsilon \approx 0.2$. So, all of our small parameters are still small, in comparison to geostrophic and hydrostatic balances. Why is there turbulence at the mesoscale?

The key has come from studying the instabilities of the quasigeostrophic equations. These equations do have a form of turbulence, quasigeostrophic turbulence (Rhines, 1979), which is very similar to two-dimensional turbulence (Kraichnan, 1967; Charney, 1971). However, unlike Kolmogorov (1941) turbulence has a *forward* energy cascade of large-scale energy toward small-scale energy, two-dimensional and quasigeostrophic turbulence has an *inverse* cascade from a central range of instability scales of energy toward *larger* scales and a forward cascade of (potential) enstrophy toward smaller scales, which is (potential) vorticity squared.

The character of turbulence and the instabilities that lead to it depend on which of the different dimensionless parameters are small, but also critically that they are equally small. Mesoscale turbulence is what occurs when the Burger number is near 1–that is, motions that are near the Rossby deformation radius. However, the mesoscale also is typified by small Rossby and Froude numbers. The mesoscale is frequently populated by the baroclinic and barotropic instabilities. The baroclinic instabilities are just a bit larger than the deformation radius in size, and the barotropic instabilities are a shear instability that forms from the horizontal shear in the boundary currents—which are also part of the mesoscale based on typical size, rotation, and stratification. The effect of latitudinal variation in the Coriolis parameter (beta-effect) is also important on the mesoscale, leading to jets in the ACC, beta-plumes, and limits on the size of the largest mesoscale eddies, but it is not required to have mesoscale turbulence. The *Rhines* scale $L_R = (V_*/\beta)^{1/2}$ is the largest scale that the beta-effect allows to be turbulent–larger scale perturbations tend to be wave-like. Not coincidentally, Charney (1955) finds that this same scale is the governing one to determine the width of inertial western boundary currents (as opposed to cruder metrics based on frictional or other parameterizations of mesoscale eddies, Stommel, 1948; Munk, 1950; Grooms et al., 2011). The quasigeostrophic equations are horizontally nondivergent at leading order, and so too are mesoscale eddies and currents, with vertical vorticity dominating their divergences.

The mesoscale is also home to many waves–Rossby waves that are subinertial like eddies, but also Kelvin, equatorial, and internal gravity. Indeed, in Fig. 2.2, the mesoscale is best identified as the region where all of the subinertial wave dispersion curves meet. Rossby wave-like features have been observed (Chelton and Schlax, 1996), but often their amplitude is so large that distinguishing waves from nonlinear waves from eddies is difficult (Chelton et al., 2007). The faster Kelvin and internal waves are more commonly observed at the mesoscale.

Until recently, global models resolving the mesoscale were rare. Through process studies and basin-scale simulations, the dynamics of the mesoscale became well-understood enough to recognize the primary behaviors of mesoscale instabilities and their effects on larger scales. In models that do not resolve the mesoscale, these behaviors are approximated with parameterizations of their effects on diffusion of tracers (Redi, 1982) and advection of buoyancy (Gent and McWilliams, 1990), as well as setting a larger horizontal viscosity to ensure numerical stability by $Re_* \sim O(1)$. The key aspects of mesoscale eddies that these parameterizations capture is that mesoscale eddies are much wider (100 km) than they are tall (4 km) so the flux more easily in the horizontal than the vertical, and their energy density is low compared to the stratification. Thus, they prefer to flow along density surfaces–or more precisely surfaces that are energetically neutral–rather than mixing together water masses of different densities which costs energy. These remedies are fairly well-understood now, and they can be made to switch off as latitudes and regional stratification vary and the mesoscale becomes resolved (Hallberg, 2013).

Submesoscales

The Rossby and Froude numbers remain small at the mesoscale while the Burger number is $O(1)$, but what happens when Rossby and Froude are not small? This is the regime known as the submesoscale. There have been many recent papers surveying the dynamics in this regime (Thomas et al., 2008; McWilliams, 2016), so only a brief summary will be included here. In Fig. 2.2 the submesoscale is indicated to be a range of scales from near the inertial period up to weeks in time, and roughly 100 m to 10 km in horizontal scale. However, it is much more accurate to define the submesoscale as the range of scales where the Rossby number and Froude number are $O(1)$. Away from the upper and bottom boundary layers of the ocean, the stratification is large on all scales and the Froude number remains small. Thus, the conditions for the *existence* of a submesoscale may only be satisfied in some layers or regions of the ocean. Given the relationship between the Burger, Rossby, and Froude numbers, this directive can be taken to indicate that the submesoscale occupies primarily the boundary layers of the ocean at scales near the mixed layer deformation radius, i.e., the deformation radius based on the stratification and width of only the mixed layer of the ocean. As the mixed layer varies seasonally, so too does the activity and scale of the submesoscale. High-resolution models and observations (Fig. 2.3) indicate that there is an active submesoscale in most surface and bottom boundary layers in most of the world at least seasonally (Mensa et al., 2013; Brannigan et al., 2015; Callies et al., 2015).

When the Rossby number is not small (58) indicates that geostrophy is no longer a good approximation. The quasigeostrophic equations are therefore no longer valid, although a number of examples of behaviors resembling mesoscale phenomena have been found to occur at the submesoscale. The submesoscale has eddies that are not geostrophic, but still are governed by a balance similar to geostrophy involving potential vorticity (Boccaletti et al., 2007). There are also fairly persistent fronts that approach geostrophic balance for the along-front velocity, even though the cross-front direction does not (Hoskins, 1975; Capet et al., 2008b). However, a critical difference between such fronts at the mesoscale and submesoscale is the strength of the cross-frontal or cross-filamentary circulation and thus the degree of surface convergence. At the mesoscale, such convergences are small, while at the submesoscale surface convergences can be as large as the vertical vorticity (D'Asaro et al., 2018). The magnitude of such convergences stems from the O (1) Rossby number effects in (35)-(40) and from an intense interaction of boundary layer mixing and frontal or filamentary convergences (McWilliams et al., 2015) or straining by submesoscale eddies and a Stokes drift effect explained below (Suzuki et al., 2016). The concentration of energy into these fronts, which then may break up into submesoscale instabilities or be dissipated by boundary layer mixing, is an important way that large-scale energy is transferred to smaller scales (Capet et al., 2008c; Callies et al., 2016), as mesoscale eddies tend to have an energy cascade toward larger scales.

Another aspect of the submesoscale, closely related to the surface convergences, is the rapid restratification due to submesoscale features (Boccaletti et al., 2007; Fox-Kemper et al., 2008; Capet et al., 2008a). While mesoscale features, particularly fronts and baroclinic eddies, do increase the stratification of the ocean by tilting horizontal density gradients into the vertical, this effect is modest and the background stratification of the ocean interior can be considered roughly independent of this effect. Submesoscale fronts and eddies, however, overturn horizontal density gradient much faster–rivaling the rate of overturning associated with geostrophic adjustment after mixing (Tandon and Garrett, 1995). An important dimensionless parameter governing restratification is the Richardson number Ri, which is closely related to the Froude number, but not identical as it depends on velocity shear not velocity magnitude:

$$\mathrm{Ri} \equiv \frac{N^2}{\frac{\partial u}{\partial z}} \sim \frac{N_*^2 H_*^2}{V_*^2} \sim \frac{V_*^2}{\left(\int_{-H}^{0} N_*(z)\, dz\right)^2} \equiv \frac{1}{\mathrm{Fr_*}^2}$$

The Richardson number indicates whether there is enough vertical shear to drive mixing and overturning of the stratification. Geostrophic adjustment can increase stratification, but it also affects the vertical shear, settling down into inertial oscillations that vary about Ri = 1. Thus, geostrophic adjustment cannot extract all of the available potential energy by overturning, just as on the planetary scale geostrophic currents balance the tendency for fronts to overturn. Symmetric instabilities are a small, fast category of submesoscale instabilities, which can also rapidly restratify toward Ri = 1 (Thomas et al., 2013; Bachman et al., 2017b). To continue restratifying beyond Ri = 1, only baroclinic instabilities (sometimes called mixed layer eddies for the submesoscale surface variety) remain. The combined effect of mixing and submesoscales is an active topic of research (Taylor and Ferrari, 2010; Hamlington et al., 2014; Whitt and Taylor, 2017; Callies and Ferrari, 2018; Sullivan and McWilliams, 2018).

Unlike the mesoscale, submesoscale dynamics allow fewer approximations in (35)-(40). Neither Rossby nor Froude numbers are small, but the aspect ratio of the submesoscale still tends to be small, so the hydrostatic approximation is usually valid. However, the quasigeostrophic equations are not valid in the submesoscale, as they require small Rossby and Froude numbers. Recall that a key advantage of the quasi-geostrophic equations was that inertial oscillations and internal gravity waves were filtered out, just as sound waves were filtered out by the Boussinesq approximation. In the submesoscale, it is not as easy to distinguish these waves from submesoscale motions exhibiting balanced dynamics–the balanced fronts and eddies exhibit convergence like waves, and their timescales are much faster and approach the timescale of these waves. For this reason, great care is needed to distinguish these wavelike and other submesoscale phenomena (Callies and Ferrari, 2013), which is a major challenge for present and planned observations and data assimilating submesoscale models.

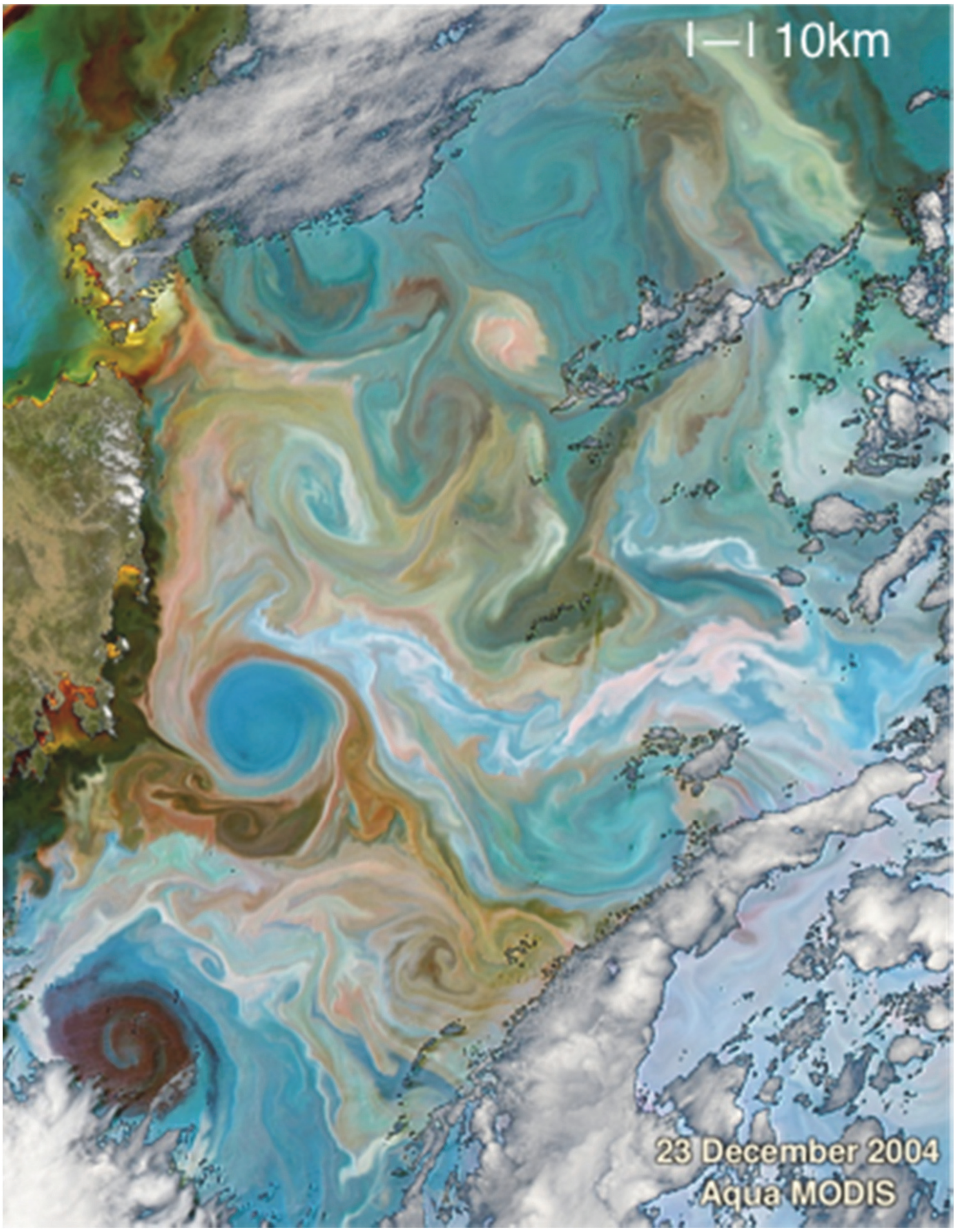

Figure 2.3. Taken from the NASA Goddard Space Flight Center Gallery: Mesoscale and submesoscale features in the Tasman Sea appear in this false color image of ocean color. The true colors from blue to green are expanded here, revealing the large mesoscale eddies (> 10 km diameter) surrounded by submesoscale fronts, filaments, and smaller (< 10 km diameter) submesoscale meanders.

A few parameterizations of submesoscale phenomena have been developed. A commonly used one seeks to capture the restratification effect of submesoscales (Fox-Kemper et al., 2008; Fox-Kemper et al., 2011) formulated as an advection similar to Gent and McWilliams (1990) with a preference for along-isopycnal transport. However, unlike the mesoscale parameterizations, which emphasized the horizontal processes, this parameterization emphasizes the vertical restratification aspect of the motions. Extensions of this parameterization and variants on these ideas remain to be implemented and tested in operational systems (Bachman and Fox-Kemper, 2013; Bachman et al., 2017c). Other submesoscale processes have been studied for parameterization purposes, such as the interaction between Ekman flow and fronts (Thomas and Lee, 2005), frontogenesis and turbulent thermal wind scalings (McWilliams, 2016), and symmetric instabilities (Bachman et al., 2017b).

Boundary layer and finescale turbulence

Long before the interest in submesoscale-convection/mixing interactions, the turbulence that mixes the upper and lower boundary layers of the ocean was recognized as important. Similarly, turbulent mixing in the ocean interior driven by breaking internal waves and tides over rough topography plays an important role in setting the stratification and overturning circulation of the abyss (Munk and Wunsch, 1998). This turbulence is similar, on its smaller scales, to isotropic three-dimensional turbulence. The aspect of this turbulence that affects larger scales and climate is its ability to overturn and mix stratification and momentum, and this overturning is naturally connected to nonhydrostatic accelerations. Thus, when this scale is reached, the final approximation to the Boussinesq equations in (35)-(40) must be abandoned (although on these small scales, sometimes planetary and Coriolis effects are neglected).

In the ocean interior away from boundary layers, mixing against stratification is a theme of the categorization of turbulence. It is the Thorpe scale–the vertical scale of the tallest well-mixed regions–and the Ozmidov scale–the largest scale at which turbulence in a stratified fluid can persist before giving way to larger-scale internal waves–that categorize turbulence.

In the boundary layers, turbulence tends to be quantified using forcing mechanisms. Wind-driven and bottom stress-driven mixing can be quantified with the friction velocity $u^*=(\tau/\rho)^{1/2}$. Langmuir turbulence, which also receives energy from surface gravity waves as well as wind, is quantified with the friction velocity and the turbulent Langmuir number which is the square root of the ratio of u^* to the Stokes drift (McWilliams et al., 1997). A third important scale is the buoyancy forcing velocity w^* = (Bsh)1/3, which measures the potential of cooling or heating at the surface to produce or suppress mixing. There are many examples of parameterizations of boundary layer mixing that take these forcings and convert them into predictions of bulk mixed layer depth (Kraus and Turner, 1967; Price et al., 1986), or predictions of vertical mixing rates (Pacanowski and Philander, 1981; Large et al., 1994; Van Roekel et al., 2012), or predictions of budgets for second moments such as variances and covariances (Mellor and Yamada, 1982; Kantha and Clayson, 2004; Harcourt, 2013), or bottom boundary layer mixing (Jayne and St Laurent, 2001; Simmons et al., 2004).

Boundary layer mixing is critically important for climate and weather modeling, as it is through these layers that the air-sea exchanges of energy, momentum, gasses (including greenhouse gasses) and moisture are exchanged. Some of the key questions that remain in the boundary layer problem are the role of waves in driving turbulence (both through breaking waves and Langmuir mixing), whether there are equation sets simpler than resolving the free surface including spray, bubbles, etc., and the details of air-sea coupling at high wind speeds where it is difficult to observe, perform experiments, and model.

Surface gravity waves

Even though surface gravity waves are (inviscid, irrotational) solutions to the Boussinesq equations with surface boundary conditions (7)-(10), for some decades wave modeling has been a separate activity from ocean interior modeling, resulting in typically separate codes, numerics, and scientific communities. However, recently these dynamics have begun to be incorporated into weather (Janssen et al. 2002) and climate (Fan and Griffies, 2014; Li et al., 2016) models, which is a step toward including their effects into a holistic portrayal of the earth system (Cavaleri et al., 2012).

Surface waves that are triggered by seismic activity or seafloor shifts are among the fastest propagating signals in the oceans. These tsunami travel at a speed of $\sqrt{gH} \approx 200$ m s^{-1}, and cross entire ocean basins in less than a day. The more common wind waves are slower and tend to adhere to nearly universal power spectra shapes governed by a combination of source functions and wave-wave interactions. Over time, wind wave energy is transferred into lower frequency swell waves, with typical wavelengths of 30 m and periods of 6 s. This assortment of waves makes for difficult modeling, but it can be combined into a prediction of the Stokes drift which is the key link between the waves, turbulence, and currents as will be described below (Webb and Fox-Kemper, 2011; 2015). Many operational oceanography systems contain a wave prediction component, but it is less common to utilize these wave predictions to force aspects of the currents and turbulence.

Examples of Reynolds-Averaged and Large Eddy Simulation Closures

The preceding sections illustrated how the governing equations can be made simpler and the phenomena one might choose to model with a tera-grid. The Boussinesq approximation eliminated sound waves, and the hydrostatic, Boussinesq equations are easier to code and more efficient than the nonhydrostatic Boussi- nesq equations. Going still further, the quasigeostrophic equations were a powerful tool in discovering the mesoscale dynamics. Just as the Boussinesq equations increase efficiency over the compressible equations by removing sound waves, the quasigeostrophic equations are vastly more efficient than the hydrostatic, Boussinesq equations. Some of the earliest proto-operational oceanography was done with the quasigeostrophic equations (e.g., Capotondi et al., 1995).

Yet, oceanographers are moving away from using these equations outside of theoretical studies. There are many reasons for this, a primary one being the availability of computing power capable of handling more complex equation sets. However, a bigger reason is that it is not only the internal waves that are missing from the quasigeostrophic equations. Quasigeostrophy limits the vertical stratification to dominate the horizontal, and the vertical stratification is not usually allowed to change within the model. This means that eddy-driven restratification, outcropping fronts, deep convection, etc., are untenable with the quasigeostrophic equations. Furthermore, converting surface forcing and topography into a meaningful form for quasigeostrophic requires a sophisticated appreciation of the asymptotic behavior of the model. As these deficits became more clear, hydrostatic Boussinesq models have become more popular, even when the dynamics at the gridscale is asymptotically consistent with quasigeostrophy (e.g., Pearson et al.,2017).

Numerical models over a limited range of scales must represent the averaged effects of smaller-scale turbulence on the resolved scales. This process can involve either Reynolds-averaging or Large Eddy Simulation style averaging (Fox-Kemper and Menemenlis, 2008). In either approach, parameterizations can be made scale-aware–that is, parameterizations adjust to the gridscale and model conditions to respond. For example, Hallberg (2013) suggests that models can evaluate the deformation radius and compare it to the grid scale. If the deformation radius and thus expected baroclinic instabilities will be resolved locally, then the Reynolds-averaged parameterization of these eddies can be turned off. If they aren't resolved locally, then leave the parameterization on. As grid scale often changes with latitude and Coriolis parameter and stratification vary, making the model aware of the dynamical scales to expect is a powerful idea. A closely related concept is flow-awareness. In this approach, the resolved flow in the model is used to inform the parameterization. Both approaches are common in Large Eddy Simulation modeling, but are not uniformly applied over all oceanographic applications, largely because parameterization systems are not well-understood for many of the tera-grids that might be chosen from Fig. 2.2.

To illustrate some of these ideas, a few example systems will be presented. The Smagorinsky (1963) classic parameterization started the idea of flow-aware, scale-aware modeling. A recent application and extension of the Leith (1996) scheme to quasigeostrophic dynamics from Bachman et al. (2017a); Pearson et al. (2017) will be used to show how important subgrid schemes can be *even at high resolution*. Finally, a discussion of the wave-averaged equations, a good example of multi-scale dynamics used to study Langmuir turbulence, will be used to motivate the inclusion of wave-current coupling in a broader range of models.

Scale-aware parameterizations

Kolmorogov & Smagorinsky 3D turbulence

Three-dimensional, nonrotating, unstratified turbulence occurs on small, fast scales in the limit of $\mathrm{Re}_* \gg 1$, $\mathrm{Fr}_* \gg 1$, $\epsilon \gg 1$, $\Delta z \sim \Delta s$, in which case we have equations (35)-(40). If we were to make a nonhydrostatic, Boussinesq model, a scale-aware LES parameterization (Kolmogorov, 1941; Smagorinsky, 1963, 1993) would be useful. The theory stems from the budget of total kinetic energy, which is the domain-average of the dot product of the momentum equations with the velocities and equal to the integral of the power spectrum $E(k)$.

$$\bar{E} = \frac{1}{2}\langle \mathbf{v} \cdot \mathbf{v} \rangle = \int_0^\infty E(k)\mathrm{d}k. \tag{52}$$

If a steady-state situation where energy is produced or otherwise injected at a rate ε on a scale far larger than the scale at which it is dissipated, then between these scales Kolmogorov (1941) argues that the energy spectrum $E(k)$ can only depend on the local scale k and ε. Dimensional analysis then demands $E(k) \propto \varepsilon^{2/3} k^{-5/3}$ and the dissipation scale is $k_d = \varepsilon^{1/4} \nu^{-3/4}$. Smagorinsky (1963, 1993) argues that in a limited resolution model, i.e., not DNS, resolved dissipation should balance the energy production, because the energy transfer through every scale in the cascade from large to small should be equal. An isotropic viscosity ν_* that can be applied to the resolved flow that has this property is

$$\nu_* = \left(\frac{\Upsilon}{k_*}\right)^2 |D_*| = \left(\frac{\Upsilon \Delta s}{\pi}\right)^2 |D_*|, \tag{53}$$

$$|D_*| = \sqrt{\frac{1}{4}\left(\frac{\partial u_{*i}}{\partial x_j} + \frac{\partial u_{*j}}{\partial x_i}\right)\left(\frac{\partial u_{*i}}{\partial x_j} + \frac{\partial u_{*j}}{\partial x_i}\right)}. \tag{54}$$

Here Υ is a dimensionless constant with a value near 1, and note that u_* is the resolved model velocity not the friction velocity u^*. Examining these equations, it is clear that even though the goal was to represent unresolved processes, there all aspects of this viscosity are known from only resolved fields–it is flow-aware. There are, of course, oversimplifications made in arriving at this simple form, but it is a robust approximation based on known behavior. Also note that the grid scale Δs appears explicitly in the formula, thus as the grid scale changes the viscosity changes automatically – it is scale-aware.

Kraichnan and Leith 2D turbulence

The eddies of the mesoscale and submesoscale are not 3D isotropic, in fact they are closer to 2D turbulence. They are much wider than they are tall, and they tend to prefer to exchange properties along isopycnals. They also conserve energy, and like 2D turbulence they conserve a form of enstrophy (vorticity squared, with power spectrum $Z(k)$). Proceeding along the same lines as Kolmogorov (1941), Kraichnan (1967) finds two different inertial ranges are consistent with these behaviors: a forward enstrophy cascade with rate η and an inverse energy cascade. If the scale of mesoscale eddy formation is resolved, then the grid scale is expected to be smaller and in the forward cascade of enstrophy, where $E(k) \propto \eta^{2/3} k^{-3}$, $Z(k) \propto \eta^{2/3} k^{-1}$, $k_d = \eta^{1/6} \nu^{-1/2}$, and energy does not cascade.

Leith (1996) follows Smagorinsky (1963, 1993) to find a viscosity to halt the enstrophy cascade:

$$\nu_* = \left(\frac{\Lambda}{k_*}\right)^3 |\nabla_h q_{z*}| = \left(\frac{\Lambda \Delta s}{\pi}\right)^3 |\nabla_h \left(f\mathbf{z} + \nabla \times \mathbf{v}_{h*}\right)|. \tag{55}$$

Here Λ is a dimensionless constant with a value near 1. Fox-Kemper and Menemenlis (2008) propose a modification to (55) to remove noisy horizontally-divergent motions.

Charney Quasigeostrophic turbulence

Quasigeostrophic theory also has an inverse energy cascade and a forward (potential) enstrophy cascade (Charney, 1971). Fig. 2.4 schematizes and illustrates the dual cascades of mesoscale turbulence in the quasigeostrophic regime.

Fox-Kemper and Menemenlis (2008) and Bachman et al. (2017a) extend the approach of Leith (1996) to apply to the potential enstrophy cascade and find,

$$\nu_* = \left(\frac{\Lambda}{k_*}\right)^3 |\nabla_h q_*| = \left(\frac{\Lambda \Delta s}{\pi}\right)^3 \left|\nabla_h(f\mathbf{z}) + \nabla_h\left(\nabla \times \mathbf{v}_{h*}\right) + \partial_z \frac{f}{N^2}\nabla_h b\right|. \quad (56)$$

As in 2D, (56) requires the extra damping of spurious divergent modes (Fox-Kemper and Menemenlis, 2008).

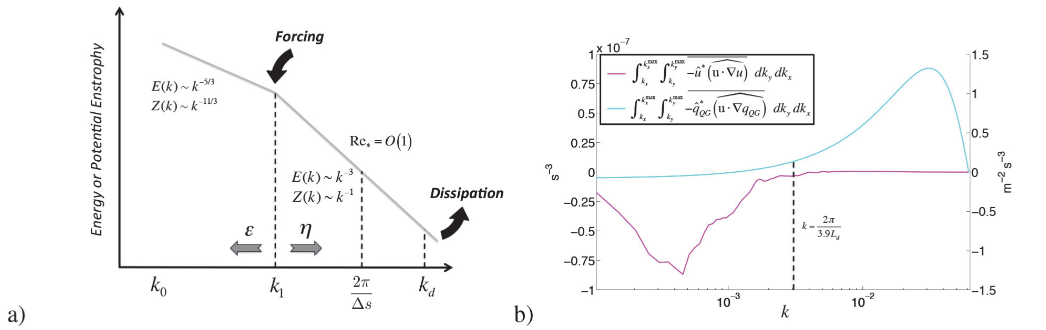

Figure 2.4. Taken from Bachman et al. (2017a): a) Schematic of the cascades of energy and potential enstrophy in quasigeostrophic flow, with spectral slopes from Smith et al. (2002). Energy and enstrophy are produced by instabilities near wavenumber k_1, leading to an inverse cascade of energy toward at the domain scale k_0 and a forward cascade of potential enstrophy toward the grid wavenumber $2\pi/\Delta s$. For a statistically steady state, a model must dissipate this energy and enstrophy appropriately. b) Spectral fluxes of (purple) energy and (blue) potential enstrophy as a function of wavelength λ, taken from a simulation with $\Delta s = L_d/10.0$, $\mathrm{Bu}_* = 100$. Negative values indicate a flux toward larger scales; positive values indicate fluxes toward smaller scales. The two cascades originate near the production scale, estimated here using the Eady (1949) fastest growing baroclinic instability wavenumber (black dashed vertical line).

Comparing the schemes

Figure 2.5 compares the average viscosity that results in the different simulations with different resolutions and subgrid models. 2D Leith tends to have the lowest average viscosity, while Smagorinsky tends to have the largest. QG Leith is systematically larger than 2D Leith, revealing that the last “stretching” term in (56) has an important effect.

Not only do the viscosities vary, the solutions vary. Fig. 2.6 shows that not only does the horizontal dissipation decrease when different subgrid schemes are used, but bottom drag increases–even though the bottom drag coefficient was unchanged. Thus, even high-resolution solutions are sensitive to changes in their parameterization of small scales.

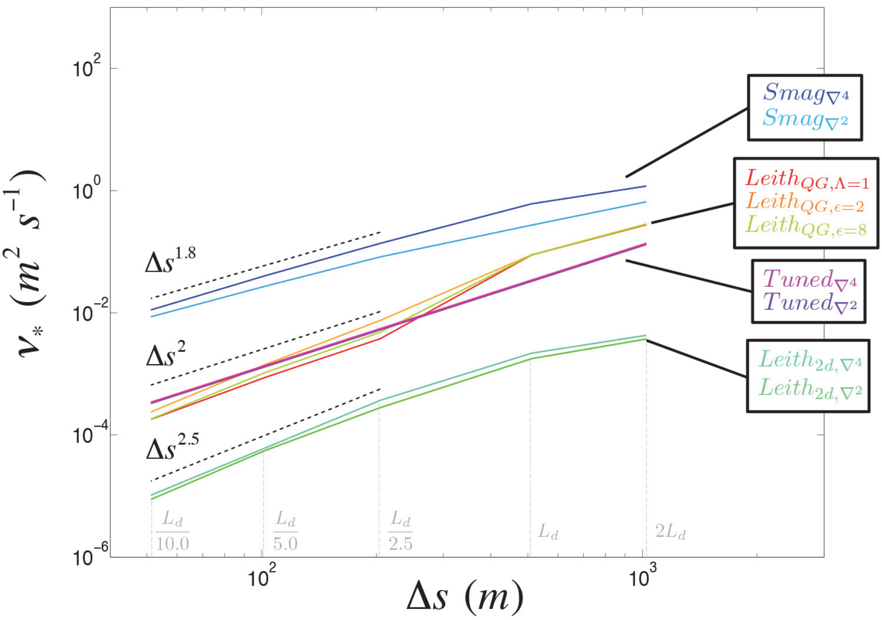

Figure 2.5. From Bachman et al. (2017a): A wide range for average viscosity (ν_*) results from using the different closures as a function of horizontal resolution (Δs). Biharmonic viscosities are shown here using the conversion factor $\nu_{2*} \approx \nu_{4*} 8/\Delta s^2$ (Griffies and Hallberg, 2000; Fox-Kemper and Menemenlis, 2008). The label above each dashed black line is its slope, which shows how the viscosity scales with resolution. The dashed grey lines indicate the resolution at which each simulation was run.

Wave-averaged equations

Not only small-scale turbulence affects the larger scales–waves do as well. Just as scales that are averaged over can contribute to larger scales through mixing, waves that are averaged over (by a period or a wavelength) can contribute to larger scales. As the discussion above indicated, one key way that spatially-dependent waves affect averaged quantities is through the Stokes drift: the difference between the Lagrangian and Eulerian velocities. Because models usually solve for the Eulerian velocities, yet conserved tracers are carried around by the Lagrangian velocity, it is important to include the Stokes drift in tracer advection. However, the Lagrangian velocity also affects the momentum equation, as it experiences a Coriolis force and a net transfer of momentum and energy from waves to currents when they are both present.

Since Craik and Leibovich (1976) showed that the Lagrangian-averaged effects of tilting vorticity by the Stokes drift shear could produce Langmuir cells, this system has been used for analysis and modeling. Notably, Holm (1996) and Gjaja and Holm (1996) improved the theoretical underpinnings by being more explicit about Lagrangian averaging, while Skyllingstad and Denbo (1995) and McWilliams et al. (1997) show that Large Eddy Simulations using the Stokes forces result in a Langmuir turbulence that qualitatively resembles observations. Even though additional work is required to add in the effects of breaking waves (Kukulka et al., 2007; Sullivan et al., 2007), D’Asaro et al. (2014) were able to verify that an LES-based scaling from Harcourt and D’Asaro (2008) does indeed seem to be a good fit to observations of vertical velocity over varying wave strengths. Other approaches to wave-driven mixing (Huang and Qiao, 2010; Babanin, 2006) based on using the wave orbital velocities to infer a Reynolds number have mixed support (Babanin and Haus, 2009; Kantha et al., 2014; Fan and Griffies, 2014). Other recent Langmuir work has broadened the scope of forcing scenarios and analysis and demonstrated that Langmuir turbulence plays an important role in the global climate system through deepening the upper ocean boundary layer (Kantha and Clayson, 2004; Van Roekel et al., 2012; Belcher et al., 2012; Fan and Griffies, 2014; Harcourt, 2013; Li et al., 2016; Li et al., 2017; Li and Fox-Kemper, 2017). These scalings for Langmuir mixing are available for operational oceanographic or climate modeling use.

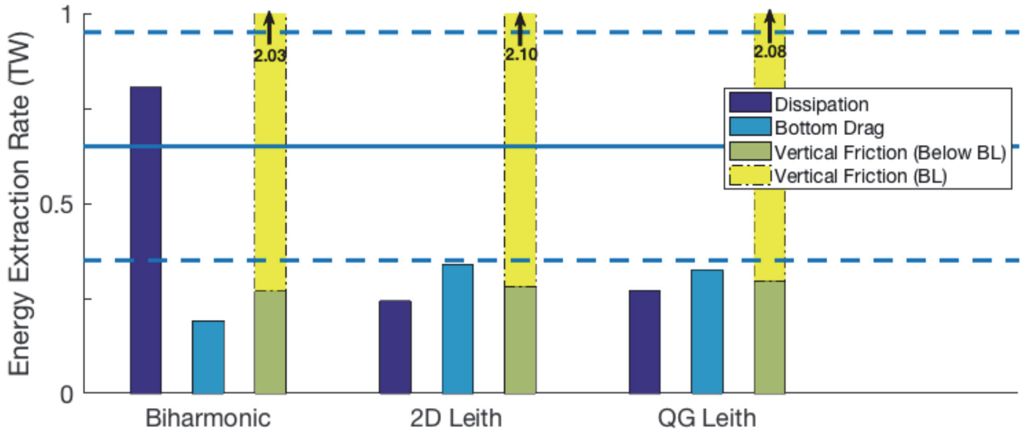

Figure 2.6. From Pearson et al. (2017): A comparison of the global integrated kinetic energy extraction by horizontal dissipation, bottom drag, vertical friction below the upper boundary layer, and vertical friction within the boundary layer in three realistically-forced, global mesoscale-resolving models.

However, Langmuir effects are not the only effect of Stokes forces on currents and turbulence. Waves have been known to affect nearshore currents and rips (e.g., Longuet-Higgins and Stewart, 1964; Uchiyama et al., 2009), to play a role in the Ekman layer (McWilliams et al., 2012), fronts (McWilliams and Fox-Kemper, 2013), submesoscale instabilities (Haney et al., 2015), and frontogenesis (Suzuki et al., 2016). The Stokes forces don't affect just Langmuir turbulence!

There are at least four schools of thought as to how to incorporate these effects. Radiation stresses are the traditional manner (Longuet-Higgins and Stewart, 1964), and the approach by Mellor (2003) is intended to simplify this approach. Fan et al. (2010) and Janssen (2004) consider the wave layer as a boundary condition capable of absorbing and releasing momentum, essentially by altering the boundary condition for wave storage. Ardhuin et al. (2008) describe the wave effect using the generalized Lagrangian mean (Andrews and McIntyre, 1978; Bühler, 2014). Another chapter in this volume addresses some of these points (Ardhuin and Orfila, 2018). Finally, the "Stokes vortex" implementation (McWilliams et al., 1997; McWilliams et al., 2004; Lane et al., 2007) has recently been shown to be inconsistent with the Mellor (2003) in theory (Ardhuin et al., 2017) and model simulations (Bennis et al., 2011; Wang et al., 2017). These discussions imply that including these forces will be an important effect, yet Breivik et al. (2015) found minimal effects when using a coarse resolution version of the NEMO ocean model. For this reason it is useful to consider the dimensionless form of the equations to see when the effects are expected to be large.

Here I will present the formulation of the Stokes forces from Suzuki and Fox-Kemper (2016), because I think they are the easiest to understand. These equations are analytically identical to the Stokes vortex formalism (McWilliams et al., 2004). Within the framework of the dimensionless equations here, it is easy to see how these forcing terms can be included into a nonhydrostatic or hydrostatic model. The wave-averaged Boussinesq momentum equation in the Suzuki and Fox-Kemper (2016) form, which solves for the Eulerian velocity **u** *averaged over wave phase in time*, are

$$\frac{\partial \mathbf{u}}{\partial t} + \underbrace{(\mathbf{u}^L \cdot \nabla)\mathbf{u}}_{\substack{\text{Lagrangian}\\ \text{advection}}} = \frac{1}{\rho_0}\nabla \cdot \left(-\pi \mathbf{I} + \sigma^{\mathrm{mol}}\right) - \underbrace{2\boldsymbol{\Omega} \times \mathbf{u}^L}_{\substack{\text{Lagrangian}\\ \text{Coriolis}}} + b\mathbf{k} - \underbrace{u_j^L \nabla u_j^S}_{\substack{\text{Stokes shear}\\ \text{force}}}, \tag{57}$$

This form of the wave-averaged Boussinesq equations frames the wave effect in terms of three forces which have distinct roles in the dynamics and energetics of wave-influenced flows; namely, the Lagrangian advection ($(\mathbf{u}^L \cdot \nabla)\mathbf{u}$), the Lagrangian Coriolis force ($\mathbf{f} \times \mathbf{u}^L$), and the Stokes shear force ($-u_j^L \nabla u_j^S$).

The dimensionless form of the Boussinesq equations, now taken to represent the wave-averaged Boussinesq equations, are

$$\mathrm{Ro}_* \left[\partial_t \mathbf{v}_h + \mathbf{v}_h^L \cdot \nabla \mathbf{v}_h + \epsilon w^L \partial_z \mathbf{v}_h + \omega_h u_j^L \partial_z u_j^S\right] = \underbrace{-\left(1 + \frac{y\mathrm{Pl}_*}{\Delta y}\right)\mathbf{z} \times \mathbf{v}_h^L - \mathrm{M}_{R*}\nabla_h \pi}_{\text{Lagrangian geostrophic}} + \frac{\mathrm{Ro}_*}{\mathrm{Re}_*}\nabla_i \sigma_{ih}, \tag{58}$$

$$\mathrm{Fr}_*^2 \frac{\Delta z^2}{\Delta s^2}\left[\partial_t w + \mathbf{v}_h^L \cdot \nabla w + \epsilon w^L \partial_z \mathbf{v}_h\right] = \underbrace{-\partial_z \pi + b - \omega_z \mathbf{u}_j^L \partial_z \mathbf{u}_j^S}_{\text{wavy hydrostatic}} + \frac{\mathrm{Fr}_*^2 \Delta z^2}{\mathrm{Re}_* \Delta s^2}\nabla_i \sigma_{iz}, \tag{59}$$

$$\partial_t S + \mathbf{v}_h^L \cdot \nabla S + \epsilon w^L \partial_z S + w^L \partial_z \bar{S} = \frac{1}{\mathrm{Pe}_*}\nabla \cdot \mathbf{I}_S^{all}, \tag{60}$$

$$\partial_t \Theta + \mathbf{v}_h^L \cdot \nabla \Theta + \epsilon w^L \partial_z \Theta + w^L \partial_z \bar{\Theta} = \frac{1}{\mathrm{Pe}_*}\nabla \cdot \mathbf{I}_\theta^{all}, \tag{61}$$

$$\partial_t b + \mathbf{v}_h^L \cdot \nabla b + \epsilon w^L \partial_z b + w^L \partial_z \bar{b} = \frac{1}{\mathrm{Pe}_*}\nabla \cdot \left(\alpha \mathbf{I}_\theta^{all} - \beta \mathbf{I}_S^{all}\right), \tag{62}$$

$$\nabla \cdot \mathbf{v}_h + \epsilon \partial_z w = 0, \tag{63}$$

$$\mathrm{M}_{R*} \equiv \max(1, \mathrm{Ro}_*), \qquad \epsilon \equiv \frac{\mathrm{Fr}_*^2}{\mathrm{Ro}_*}\mathrm{M}_{R*} = \begin{cases} \mathrm{Fr}_*^2 & \mathrm{Ro}_* \geq 1, \\ \mathrm{Ro}_* \mathrm{Bu}_*^{-1} & \mathrm{Ro}_* < 1 \end{cases} \tag{64}$$

The wave parameters $\omega_h = \frac{V^S}{V^L}\frac{\Delta s}{L^S}$ and $\omega_z = \frac{V^S}{V^L}\frac{\Delta z}{H^S}$ min (1, Ro$_*$) categorize the strength of the Stokes shear force in the horizontal and vertical momentum equations, respectively. Generally, ω_h is small, as Stokes drift is slightly weaker than the Lagrangian velocity and varies slowly in the horizontal.

However, ω_z is $O(1)$ for Langmuir, submesoscale, and strong mesoscale flows, which means that not only does the Stokes force drive Langmuir circulations, but *the Stokes shear force contributes as much as the buoyancy in forcing the strengthening of fronts by enhancing the downward part of their frontogenetic secondary circulation* (Suzuki and Fox-Kemper, 2016). The essential example of this force is shown in Fig. 2.7, where a surface jet (in the Langmuir case) or front (in the submesoscale case) is aligned with the direction of the surface Stokes drift. As the

Stokes drift decays with depth, the Stokes shear force is downward in the center of the jet or front. A downward force at this point tends to enhance the strength of the jet or front, which in turn leads to more Stokes shear force, etc. This mechanism is the same mathematically as the primary mechanism explained by Craik and Leibovich (1976) for Langmuir circulations, but it is simpler and also applies equally well to the frontal case. Furthermore, as the Stokes shear force depends on the match in direction between fronts and the Stokes drift, it predicts that Langmuir cells will orient downwind and that up-Stokes fronts will be weakened while down-Stokes fronts are enhanced. Suzuki et al. (2016) show that in a submesoscale-resolving simulation including Stokes drift, this effect is strong, accounting for the equivalent of 40% of the buoyancy effects in forming a front. Even in hydrostatic models, the Stokes shear force can be included, and it will affect the pressure field of currents that are aligned with the wave direction. It is easy to include, by including it wherever the buoyancy appears. Fig. 2.7 schematizes the effect of this term.

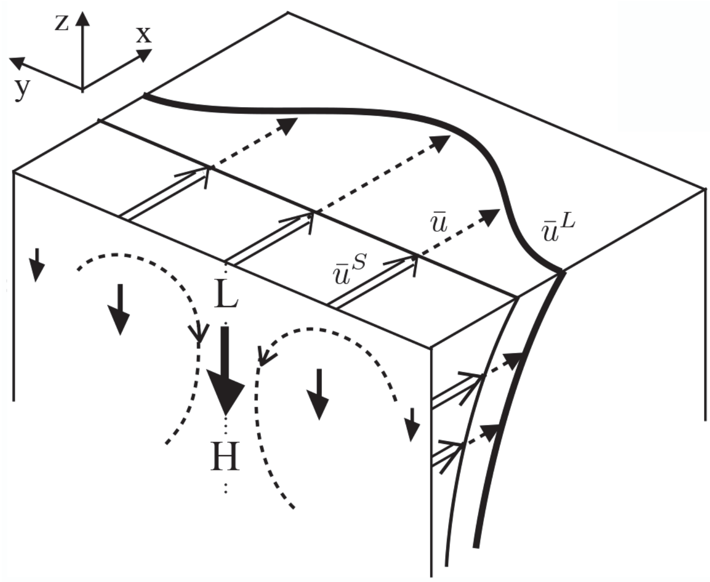

Figure 2.7. From Suzuki and Fox-Kemper (2016): This schematic illustrates how the Stokes shear force can drive, defeat, or enhance a secondary circulation related to a surface jet (i.e., a Langmuir cell) or front (and its associated secondary circulation). In this example, the jet or front is oriented along the direction of the Stokes shear, causing a strong downward acceleration in the middle of the feature. To either side, the velocity is weaker and thus the downward Stokes shear force is weaker, even though the Stokes drift is horizontally uniform.

One final comment on the wave averaged equations. Sometimes the effects of Stokes drift are estimated by only including Stokes advection without adding Stokes Coriolis or Stokes shear force to the momentum equation (e.g., McWilliams and Restrepo, 1999; Breivik et al., 2015; Curcic et al., 2016). This is almost certainly an overestimate of the Stokes effects, because the Stokes forces frequently act to make the Lagrangian advection similar to the Eulerian advection when no Stokes forces are present (Monismith et al., 2007; Lentz and Fewings, 2012; McWilliams and Fox-Kemper, 2013).

Conclusions

Although the oceans are vast and diverse, like a giant aquarium filled with interesting dynamical phenomena, much progress has been made in modeling the variability. Although computation is limited to roughly a few tera-grids and will expand only modestly during our lifetimes, there is much that can be done with this amount of computation. Rather than solving the fundamental equations of compressible fluid dynamics with molecular effects, approximations to these equations can be made.

The Boussinesq approximation filters sound waves, allowing longer time steps. The quasigeostrophic equations filter gravity waves for longer time steps still, although these equations are limited to use on the extratropical mesoscales only. The wave-averaged equations are less expensive than resolving waves, but require Stokes forces be introduced as a parameterization of leading wave effects. These wave effects are at the root of Langmuir turbulence, but also have profound effects in coastal regions and on submesoscale dynamics.

Other parameterizations can be formulated–for mesoscale eddies, submesoscale eddies, boundary layer mixing, etc. It is particularly helpful when these parameterizations are scale-aware and flow-aware, as this means that they do not require tuning and can respond differently and appropriately in different regimes across the globe. Dimensionless equations and dimensionless parameters can help decide how and where to make these adjustments. The Smagorinsky, Leith, and QG Leith schemes demonstrate how different dynamics at the gridscale affect the parameterization choice that is optimal, and comparing matching simulations varying only the choice of parameterizations demonstrates the influence of this choice even in high-resolution simulations.

References

Andrews, D. G. and M. E. McIntyre: 1978, An exact theory of nonlinear waves on a Lagrangian-mean flow. *Journal of Fluid Mechanics*, **89**, 609–646.

Ardhuin, F. and A. Orfila: 2018, Wind waves. *GODAE Book*.

Ardhuin, F., N. Rascle, and K. A. Belibassakis: 2008, Explicit wave-averaged primitive equations using a generalized Lagrangian mean. *Ocean Modelling*, **20**, 35–60.

Ardhuin, F., N. Suzuki, J. C. McWilliams, and H. Aiki: 2017, Comments on “a combined derivation of the integrated and vertically resolved, coupled wave-current equations”. *Journal of Physical Oceanography,* **47**(9):2377–2385, URL http://dx.doi.org/10.1175/JPO-D-17-0065.1.

Babanin, A.: 2006, On a wave-induced turbulence and a wave-mixed upper ocean layer. *Geophysical Research Letters*, **33**, L20605, URL http://dx.doi.org/10.1029/2006GL027308.

Babanin, A. V. and B. K. Haus: 2009, On the existence of water turbulence induced by nonbreaking surface waves. *Journal of Physical Oceanography*, **39**.

Bachman, S. and B. Fox-Kemper: 2013, Eddy parameterization challenge suite. I: Eady spindown. *Ocean Modelling*, **64**, 12–28. URL http://dx.doi.org/10.1016/j.ocemod.2012.12.003

Bachman, S. D., B. Fox-Kemper, and B. Pearson: 2017a, A scale-aware subgrid model for quasigeostrophic turbulence. *Journal of Geophysical Research–Oceans*, **122**, 1529–1554. URL http://dx.doi.org/10.1002/2016JC012265

Bachman, S. D., B. Fox-Kemper, J. R. Taylor, and L. N. Thomas: 2017b, Parameterization of frontal symmetric instabilities. I: Theory for resolved fronts. *Ocean Modelling*, **109**, 72–95. URL http://dx.doi.org/10.1016/j.ocemod.2016.12.003

Bachman, S. D., D. P. Marshall, J. R. Maddison, and J. Mak: 2017c, Evaluation of a scalar eddy transport coefficient based on geometric constraints. *Ocean Modelling*, **109**, 44–54. URL http://dx.doi.org/10.1016/j.ocemod.2016.12.004

Barkan, R., J. C. McWilliams, M. J. Molemaker, J. Choi, K. Srinivasan, A. F. Shchepetkin, and A. Bracco: 2017, Submesoscale dynamics in the northern gulf of mexico. Part II: Temperature-salinity relations and cross shelf transport processes. *Journal of Physical Oceanography*.

Bates, S. C., B. Fox-Kemper, S. R. Jayne, W. G. Large, S. Stevenson, and S. G. Yeager: 2012, Mean biases, variability, and trends in air-sea fluxes and SST in the CCSM4. *Journal of Climate*, **25**, 7781–7801. URL http://dx.doi.org/10.1175/JCLI-D-11-00442.1

Belcher, S. E., A. A. L. M. Grant, K. E. Hanley, B. Fox-Kemper, L. Van Roekel, P. P. Sullivan, W. G. Large, A. Brown, A. Hines, D. Calvert, A. Rutgersson, H. Petterson, J. Bidlot, P. A. E. M. Janssen, and J. A. Polton: 2012, A global perspective on Langmuir turbulence in the ocean surface boundary layer. *Geophysical Research Letters*, **39**, L18605, 9pp. URL http://dx.doi.org/10.1029/2012GL052932

Bennis, A.-C., F. Ardhuin, and F. Dumas: 2011, On the coupling of wave and three-dimensional circulation models: Choice of theoretical framework, practical implementation and adiabatic tests. *Ocean Modelling*, **40**, 260–272.

Boccaletti, G., R. Ferrari, and B. Fox-Kemper: 2007, Mixed layer instabilities and restratification. *Journal of Physical Oceanography*, **37**, 2228–2250. URL http://dx.doi.org/10.1175/JPO3101.1

Boussinesq, J.: 1897, *Théorie de l'e´coulmnent tourbillonnant et tumultuex des liquides dans les lits rectilignes à grande section*, volume 1. Gauthier-Villars.

Brannigan, L., D. P. Marshall, A. Naveira-Garabato, and A. G. Nurser: 2015, The seasonal cycle of submesoscale flows. *Ocean Modelling*, **92**, 69–84.

Breivik, O., K. Mogensen, J.-R. Bidlot, M. A. Balmaseda, and P. A. Janssen: 2015, Surface wave effects in the NEMO ocean model: Forced and coupled experiments. *Journal of Geophysical Research: Oceans*.

Bühler, O.: 2014, Waves *and mean flows*. Cambridge monographs on mechanics, Cambridge University Press, Cambridge, United Kingdom, second edition.

Caldwell, D. and S. Eide: 1981, Soret coefficient and isothermal diffusivity of aqueous solutions of five principal salt constituents of seawater. *Deep Sea Research Part A. Oceanographic Research Papers*, **28**, 605–1618.

Callies, J. and R. Ferrari: 2013, Interpreting energy and tracer spectra of upper-ocean turbulence in the submesoscale range (1–200 km). *Journal of Physical Oceanography*, **43**, 2456–2474.

Callies, J.: 2018, Baroclinic instability in the presence of convection. *Journal of Physical Oceanography*, **48**, 45–60.

Callies, J., R. Ferrari, J. M. Klymak, and J. Gula: 2015, Seasonality in submesoscale turbulence. *Nature communications*, **6**, 6862.

Callies, J., G. Flierl, R. Ferrari, and B. Fox-Kemper: 2016, The role of mixed layer instabilities in submesoscale turbulence. *Journal of Fluid Mechanics*, **788**, 5–41. URL http://dx.doi.org/10.1017/jfm.2015.700

Capet, X., J. C. Mcwilliams, M. J. Mokemaker, and A. F. Shchepetkin: 2008a, Mesoscale to submesoscale transition in the California current system. Part I: Flow structure, eddy flux, and observational tests. *Journal of Physical Oceanography*, **38**, 29–43.

Capet, X., J. C. Mcwilliams, M. J. Molemaker, and A. F. Shchepetkin: 2008b, Mesoscale to submesoscale transition in the California current system. Part II: Frontal processes. *Journal of Physical Oceanography*, **38**, 44–64.

Capet, X., J. C. McWilliams, M. J. Molemaker, and A. F. Shchepetkin: 2008c, Mesoscale to submesoscale transition in the California current system. part III Energy balance and flux. *Journal of Physical Oceanography*, **38**, 2256–2269.

Capotondi, A., P. Malanotte-Rizzoli, and W. R. Holland: 1995, Assimilation of altimeter data into a quasi-geostrophic model of the gulf-stream system .1. dynamical considerations.

Cavaleri, L., B. Fox-Kemper, and M. Hemer: 2012, Wind waves in the coupled climate system. *Bulletin of the American Meteorological Society*, **93**, 1651–1661. URL http://dx.doi.org/10.1175/BAMS-D-11-00170.1

Charney, J. G.: 1955, The Gulf Stream as an inertial boundary layer. *Proceedings of the National Academy of Sciences*, **41**, 731–740.

— 1971, Geostrophic turbulence. *Journal of the Atmospheric Sciences*, **28**, 1087–1095.

Charney, J. G., R. Fjörtoft, and J. V. Neumann: 1950, Numerical integration of the barotropic vorticity equation. *Tellus*, **2**, 237–254.

Chelton, D., M. Schlax, R. Samelson, and R. de Szoeke: 2007, Global observations of large oceanic eddies. *Geophysical Research Letters*, **34**, L15606.

Chelton, D. B., R. A. Deszoeke, and M. G. Schlax: 1998, Geographical variability of the first baroclinic Rossby radius of deformation. *Journal of Physical Oceanography*, **28**, 433–460.

Chelton, D. B. and M. G. Schlax: 1996, Global observations of oceanic Rossby waves. *Science*, **272**, 234– 238.

Chen, C., I. Kamenkovich, and P. Berloff: 2016, Eddy trains and striations in quasigeostrophic simulations and the ocean. *Journal of Physical Oceanography*, **46**, 2807–2825.

Corrsin, S.: 1951, On the spectrum of isotropic temperature fluctuations in an isotropic turbulence. *Journal of Applied Physics*, **22**, 469–473.

Craik, A. D. D. and S. Leibovich: 1976, Rational model for Langmuir circulations. *Journal of Fluid Mechanics*, **73**, 401–426.

Curcic, M., S. S. Chen, and T. M. O¨ zgo¨kmen: 2016, Hurricane-induced ocean waves and stokes drift and their impacts on surface transport and dispersion in the Gulf of Mexico. *Geophysical Research Letters*, **43**, 2773–2781.

D'Asaro, E. A., A. Y. Shcherbina, J. M. Klymak, J. Molemaker, G. Novelli, C. M. Guigand, A. C. Haza,

Haus, B. K., E. H. Ryan, G. A. Jacobs, et al.: 2018, Ocean convergence and the dispersion of flotsam. *Proceedings of the National Academy of Sciences*, 201718453.

D'Asaro, E. A., J. Thomson, A. Y. Shcherbina, R. R. Harcourt, M. F. Cronin, M. A. Hemer, and B. Fox-Kemper: 2014, Quantifying upper ocean turbulence driven by surface waves. *Geophysical Research Letters*, **41**, 102–107. URL http://dx.doi.org/10.1002/2013GL058193

Deardorff, J.: 1970, A numerical study of three-dimensional turbulent channel flow at large Reynolds numbers. *Journal of Fluid Mechanics*, **41**, 453–480.

Deser, C., A. Capotondi, R. Saravanan, and A. Phillips: 2006, Tropical Pacific and Atlantic climate variability in CCSM3. *J. Clim.*, **19**, 2451–2481.

Eady, E. T.: 1949, Long waves and cyclone waves. *Tellus*, **1**, 33–52.

Ekman, V. W.: 1905, On the influence of the Earth's rotation on ocean currents. *Arkiv. Mat. Astron. Fysik.*, **2**, 1–53.

Euler, L.: 1757, Principes generaux du mouvement des fluides. *Mémoires de l'Academie des Sciences de Berlin*, **11**, 274–315.

Fan, Y., I. Ginis, and T. Hara: 2010, Momentum flux budget across the air–sea interface under uniform and tropical cyclone winds. *Journal of Physical Oceanography*, **40**, 2221–2242.

Fan, Y. and S. M. Griffies: 2014, Impacts of parameterized langmuir turbulence and non-breaking wave mixing in global climate simulations. *Journal of Climate*, in press.

Fermi, E.: 1956, *Thermodynamics*. Dover, new edition, 176 pp. Fick, A.: 1855, Ueber diffusion. *Annalen der Physik*, **170**, 59–86.

Fofonoff, N. P.: 1954, Steady flow in a frictionless homogenous ocean. *Journal of Marine Research*, **13**, 254–262.

Fourier, J.: 1822, *Theorie analytique de la chaleur, par M. Fourier*. Chez Firmin Didot, père et fils.

Fox-Kemper, B., S. Bachman, B. Pearson, and S. Reckinger: 2014, Principles and advances in subgrid modeling for eddy-rich simulations. *CLIVAR Exchanges*, **19**, 42–46. URL http://bit.ly/1qSMTzA

Fox-Kemper, B., G. Danabasoglu, R. Ferrari, S. M. Griffies, R. W. Hallberg, M. M. Holland, M. E. Maltrud, S. Peacock, and B. L. Samuels: 2011, Parameterization of mixed layer eddies. III: Implementation and impact in global ocean climate simulations. *Ocean Modelling*, **39**, 61–78. URL http://dx.doi.org/10.1016/j.ocemod.2010.09.002

Fox-Kemper, B. and R. Ferrari: 2009, An eddifying Parsons model. *Journal of Physical Oceanography*, **39**, 3216–3227. URL http://ams.allenpress.com/perlserv/?request=get-abstract&doi=10.1175%2F2009JPO4104.1

Fox-Kemper, B., R. Ferrari, and R. Hallberg: 2008, Parameterization of mixed layer eddies. Part I: Theory and diagnosis. *Journal of Physical Oceanography*, **38**, 1145–1165. URL http://dx.doi.org/10.1175/2007JPO3792.1

Fox-Kemper, B. and D. Menemenlis: 2008, Can large eddy simulation techniques improve mesoscale-rich ocean models? *Ocean Modeling in an Eddying Regime*, M. Hecht and H. Hasumi, eds., AGU Geophysical Monograph Series, volume 177, 319–338.

Fox-Kemper, B. and J. Pedlosky: 2004, Wind-driven barotropic gyre I: Circulation control by eddy vorticity fluxes to an enhanced removal region. *Journal of Marine Research*, **62**, 169–193. URL http://www.ingentaselect.com/rpsv/cgi-bin/cgi?body=linker&reqidx=0022-2402(20040301)62:2L.169;1-

Frankignoul, C. and K. Hasselmann: 1977, Stochastic climate models. II: Application to sea surface temperature variability and thermocline variability. *Tellus*, **29**, 284–305.

Frenger, I., N. Gruber, R. Knutti, and M. Münnich: 2013, Imprint of southern ocean eddies on winds, clouds and rainfall. *Nature Geoscience*, **6**, 608–612.

Gebbie, G. and P. Huybers: 2012, The mean age of ocean waters inferred from radiocarbon observations: sensitivity to surface sources and accounting for mixing histories. *Journal of Physical Oceanography*, **42**, 291–305.

Gent, P. R. and J. C. McWilliams: 1990, Isopycnal mixing in ocean circulation models. *Journal of Physical Oceanography*, **20**, 150–155.

Gjaja, I. and D. Holm: 1996, Self-consistent hamiltonian dynamics of wave mean-flow interaction for a rotating stratified incompressible fluid. *Physica D*, **98**, 343–378.

Gnanadesikan, A.: 1999, A simple predictive model for the structure of the oceanic pycnocline. *Science*, **283**, 2077–2079.

Griffies, S. and R. Hallberg: 2000, Biharmonic friction with a Smagorinsky-like viscosity for use in largescale eddy-permitting ocean models. *Monthly Weather Review*, **128**, 2935–2946.

Griffies, S. M. and R. J. Greatbatch: 2012, Physical processes that impact the evolution of global mean sea level in ocean climate models. *Ocean Modelling*, **51**, 37–72.

Grist, J. P. and S. A. Josey: 2003, Inverse analysis adjustment of the SOC air–sea flux climatology using ocean heat transport constraints. *Journal of Climate*, **16**, 3274–3295.

Grooms, I., K. Julien, and B. Fox-Kemper: 2011, On the interactions between planetary geostrophy and mesoscale eddies. *Dynamics of Atmospheres and Oceans*, **51**, 109–136. URL http://dx.doi.org/10.1016/j.dynatmoce.2011.02.002

Haidvogel, D., E. Churchitser, S. Danilov, and B. Fox-Kemper: 2017, Multiscale multi-physics ocean modeling: Numerics (invited). *The Sea*, Journal of Marine Research, in press. URL http://bit.ly/2BnSdaQ

Hallberg, R.: 2013, Using a resolution function to regulate parameterizations of oceanic mesoscale eddy effects. *Ocean Modelling*, **72**, 92–103.

Hamlington, P. E., L. P. Van Roekel, B. Fox-Kemper, K. Julien, and G. P. Chini: 2014, Langmuir-submesoscale interactions: Descriptive analysis of multiscale frontal spin-down simulations. *Journal of Physical Oceanography*, **44**, 2249–2272. URL http://dx.doi.org/10.1175/JPO-D-13-0139.1

Haney, S., B. Fox-Kemper, K. Julien, and A. Webb: 2015, Symmetric and geostrophic instabilities in the wave-forced ocean mixed layer. *Journal of Physical Oceanography*, **45**, 3033–3056. URL http://dx.doi.org/10.1175/JPO-D-15-0044.1

Hansen, J., M. Sato, P. Kharecha, and K. v. Schuckmann: 2011, Earth's energy imbalance and implications. *Atmospheric Chemistry and Physics*, **11**, 13421–13449.

Harcourt, R. R.: 2013, A second-moment closure model of langmuir turbulence. *Journal of Physical Oceanography*, **43**.

Harcourt, R. R. and E. A. D'Asaro: 2008, Large-eddy simulation of Langmuir turbulence in pure wind seas. *Journal of Physical Oceanography*, **38**, 1542–1562.

Hasselmann, K.: 1976, Stochastic climate models. Part I: Theory. *Tellus*, **28**, 473–485.

Held, I. M. and T. Schneider: 1999, The surface branch of the zonally averaged mass transport circulation in the troposphere. *Journal of the Atmospheric Sciences*, **56**, 1688–1697.

Holm, D.: 1996, The ideal Craik-Leibovich equations. *Physica D*, **98**, 415–441.

Hoskins, B. J.: 1975, The geostrophic momentum approximation and the semi-geostrophic equations. *Journal of the Atmospheric Sciences*, **32**, 233–242.

Huang, C. J. and F. Qiao: 2010, Wave-turbulence interaction and its induced mixing in the upper ocean. *Journal of Geophysical Research: Oceans*, **115**.

Huang, R. X. and G. R. Flierl: 1987, Two-layer models for the thermocline and current structure in subtropical/subpolar gyres.

Jansen, M. F. and I. M. Held: 2014, Parameterizing subgrid-scale eddy effects using energetically consistent backscatter. *Ocean Modelling*, **80**, 36–48.

Janssen, P.A.E.M., J. D. Doyle, J. Bidlot, B. Hansen, L. Isaksen, and P. Viterbo. Impact and feedback of ocean waves on the atmosphere. In W. Perrie, editor, *Adv. Fluid. Mech.*, volume I of *Atmosphere–Ocean Interactions*. 2002.

Janssen, P.: 2004, *The interaction of ocean waves and wind*. Cambridge University Press.

Jayne, S. and L. St Laurent: 2001, Parameterizing tidal dissipation over rough topography. *Geophysical Research Letters*, **28**, 811–814.

Johnson, G. C. and H. L. Bryden: 1989, On the size of the Antarctic Circumpolar Current. *Deep-Sea Research Part A-Oceanographic Research Papers*, **36**, 39–53.

Julien, K., E. Knobloch, R. Milliff, and J. Werne: 2006, Generalized quasi-geostrophy for spatially anisotropic rotationally constrained flows. *Journal of Fluid Mechanics*, **555**, 233–274.

Kantha, L. and C. Clayson: 2004, On the effect of surface gravity waves on mixing in the oceanic mixed layer. *Ocean Modelling*, **6**, 101–124.

Kantha, L., H. Tamura, and Y. Miyazawa: 2014, Comment on "wave-turbulence interaction and its induced mixing in the upper ocean" by Huang and Qiao. *Journal of Geophysical Research: Oceans*, **119**, 1510–1515.

Karsten, R. H. and J. Marshall: 2002, Constructing the residual circulation of the acc from observations. *Journal of physical oceanography*, **32**, 3315–3327.

Kolmogorov, A. N.: 1941, The local structure of turbulence in incrompressible viscous fluid for very large reynolds number. *Dokl. Akad. Nauk. SSSR*, **30**, 9–13.

Kourafalou, V., P. De Mey, M. Le He´naff, G. Charria, C. Edwards, R. He, M. Herzfeld, A. Pascual, E. Stanev, J. Tintore´, et al.: 2015, Coastal ocean forecasting: system integration and evaluation. *Journal of Operational Oceanography*, **8**, s127–s146.

Kraichnan, R. H.: 1967, Inertial ranges in two-dimensional turbulence. *Physics of Fluids*, **16**, 1417–1423.

Kraus, E. and J. Turner: 1967, A one-dimensional model of the seasonal thermocline. II: The general theory and its consequences. *Tellus*, **19**, 98–106.

Kukulka, T., T. Hara, and S. E. Belcher: 2007, A model of the air-sea momentum flux and breaking-wave distribution for strongly forced wind waves. *Journal of Physical Oceanography*, **37**, 1811–1828.

Lane, E. M., J. M. Restrepo, and J. C. McWilliams: 2007, Wave-current interaction: A comparison of radiation-stress and vortex-force representations. *Journal of Physical Oceanography*, **37**, 1122–1141.

Laplace, P. S., N. Bowditch, and N. I. Bowditch: 1829, *Mécanique céleste*. Hillard, Gray, Little, and Wilkins, Boston.

Large, W. G., J. C. McWilliams, and S. C. Doney: 1994, Oceanic vertical mixing a review and a model with a nonlocal boundary-layer parameterization. *Reviews of Geophysics*, **32**, 363–403.

LeBlond, P. H. and L. A. Mysak: 1978, *Waves in the Ocean*. Number 20 in Elsevier Oceanography, Elsevier Scientific Publishing Company, New York.

Leith, C. E.: 1996, Stochastic models of chaotic systems. *Physica D*, **98**, 481–491.

Lentz, S. J. and M. R. Fewings: 2012, The wind-and wave-driven inner-shelf circulation. *Annual review of marine science*, **4**, 317–343.

Li, Q., B. Fox-Kemper, O. Breivik, and A. Webb: 2017, Statistical modeling of global Langmuir mixing. *Ocean Modelling*, **113**, 95–114. URL http://dx.doi.org/10.1016/j.ocemod.2017.03.016

Li, Q. and B. Fox-Kemper: 2017, Assessing the effects of Langmuir turbulence on the entrainment buoyancy flux in the ocean surface boundary layer. *Journal of Physical Oceanography*, in press. URL http://bit.ly/2otyrUT

Li, Q., A. Webb, B. Fox-Kemper, A. Craig, G. Danabasoglu, W. G. Large, and M. Vertenstein: 2016, Langmuir mixing effects on global climate: WAVEWATCH III in CESM. *Ocean Modelling*, **103**, 145– 160. URL http://dx.doi.org/10.1016/j.ocemod.2015.07.020

Lilly, D. K.: 1983, Stratified turbulence and the mesoscale variability of the atmosphere. *Journal of the Atmospheric Sciences*, **40**, 749–761.

Longuet-Higgins, M. S. and R. W. Stewart: 1964, Radiation stresses in water waves: A physical discussion, with applications. *Deep Sea Res.*, **11**, 529–562.

Lozier, M. S.: 2010, Deconstructing the conveyor belt. *Science*, **328**, 1507–1511.

Luyten, J. R., J. Pedlosky, and H. Stommel: 1983, The ventilated thermocline. *Journal of Physical Oceanography*, **13**, 292–309.

Maltrud, M. E. and J. L. McClean: 2005, An eddy resolving global 1/10◦ ocean simulation. *Ocean Modelling*, **8**, 31–54.

Marangoni, C.: 1865, *Sull'espansione delle goccie d'un liquido galleggianti sulla superfice di altro liquido*. Fratelli Fusi, Pavia, Italy.

McDougall, T.: 2003, Potential enthalpy: A conservative oceanic variable for evaluating heat content and heat fluxes. *Journal of Physical Oceanography*, **33**, 945–963.

McDougall, T. J. and P. M. Barker: 2011, Getting started with teos-10 and the gibbs seawater (gsw) oceanographic toolbox. *SCOR/IAPSO WG*, **127**, 1–28.

McWilliams, J. and J. Restrepo: 1999, The wave-driven ocean circulation. *Journal of Physical Oceanography*, **29**, 2523–2540.

McWilliams, J., J. Restrepo, and E. Lane: 2004, An asymptotic theory for the interaction of waves and currents in coastal waters. *Journal of Fluid Mechanics*, **511**, 135–178.

McWilliams, J. C.: 1985, A uniformly valid model spanning the regimes of geostrophic and isotropic, stratified turbulence: Balanced turbulence. *Journal of the Atmospheric Sciences*, **42**, 1773–1774.

— 2016, Submesoscale currents in the ocean. *Proc. R. Soc. A*, The Royal Society, volume 472, 20160117.

McWilliams, J. C. and B. Fox-Kemper: 2013, Oceanic wave-balanced surface fronts and filaments. *Journal of Fluid Mechanics*, **730**, 464–490. URL http://dx.doi.org/10.1017/jfm.2013.348

McWilliams, J. C., J. Gula, M. J. Molemaker, L. Renault, and A. F. Shchepetkin: 2015, Filament frontogenesis by boundary layer turbulence. *Journal of Physical Oceanography*, **45**, 1988–2005.

McWilliams, J. C., E. Huckle, J.-H. Liang, and P. P. Sullivan: 2012, The wavy Ekman layer: Langmuir circulations, breaking waves, and reynolds stress. *Journal of Physical Oceanography*, **42**, 1793–1816.

McWilliams, J. C., P. P. Sullivan, and C.-H. Moeng: 1997, Langmuir turbulence in the ocean. *Journal of Fluid Mechanics*, **334**, 1–30.

Meehl, G. A., L. Goddard, G. Boer, R. Burgman, G. Branstator, C. Cassou, S. Corti, G. Danabasoglu, F. Doblas-Reyes, E. Hawkins, et al.: 2014, Decadal climate prediction: an update from the trenches. *Bulletin of the American Meteorological Society*, **95**, 243–267.

Mellor, G.: 2003, The three-dimensional current and surface wave equations. *Journal of Physical Oceanography*, **33**, 1978–1989.

Mellor, G. L. and T. Yamada: 1982, Development of a turbulent closure model for geophysical fluid problems. **20**, 851–857.

Mensa, J. A., Z. Garraffo, A. Griffa, T. M. O¨ zgo¨kmen, A. Haza, and M. Veneziani: 2013, Seasonality of the submesoscale dynamics in the gulf stream region. *Ocean Dynamics*, **63**, 923–941.

Milankovitch, M.: 1930, Mathematische klimalehre und astronomische theorie der klimashwankungengebruder borntraeger.

Monismith, S. G., E. A. Cowen, H. M. Nepf, J. Magnadaudet, and L. Thais: 2007, Laboratory observations of mean flows under surface gravity waves. *Journal of Fluid Mechanics*, **573**, 131–147.

Moore, G. E.: 1965, Cramming more components onto integrated circuits. *Electronics*, **38**, 114–117. Mu¨ller, P.: 2006, *The equations of oceanic motions*. Cambridge University Press.

Munk, W. and C. Wunsch: 1998, Abyssal recipes ii: energetics of tidal and wind mixing. *Deep-Sea Research Part I-Oceanographic Research Papers*, **45**, 1977–2010.

Munk, W. H.: 1950, On the wind-driven ocean circulation. *Journal of Meteorology*, **7**, 79–93.

Navier, C.-L.: 1822, Me´moire sur les lois du mouvement des fluides. *Mem. de l'Acad. des Sciences*, **389**. Nazarenko, S.: 2011, *Wave turbulence*, volume 825. Springer Science & Business Media.

NOAA, N.: 2018, State of the climate: Global climate report for annual 2017. URL https://www.ncdc.noaa.gov/sotc/global/201713

Obukhov, A.: 1949, Structure of the temperature field in turbulent flow. *Izvestiia Akademii M!auk S.S.S.R.*, **13**, 58–69, translation (from Russian) No. 334 by Army Biological Labs, 1968.

Olbers, D. and C. Eden: 2003, A simplified general circulation model for a baroclinic ocean with topography. part I: Theory, waves, and wind-driven circulations. *Journal of Physical Oceanography*, **33**, 2719–2737.

Onsager, L.: 1931a, Reciprocal relations in irreversible processes. i. *Physical review*, **37**, 405.

— 1931b, Reciprocal relations in irreversible processes. ii. *Physical review*, **38**, 2265.

Pacanowski, R. and S. Philander: 1981, Parameterization of vertical mixing in numerical models of tropical oceans. *J. Phys. Ocean.*, **11**, 1443–1451.

Pauluis, O.: 2011, Water vapor and mechanical work: A comparison of Carnot and steam cycles. *Journal of the Atmospheric Sciences*, **68**, 91–102.

Pearson, B. and B. Fox-Kemper: 2018, Lognormal turbulence dissipation in global ocean models. *Physical Review Letters*, in press. URL http://bit.ly/2A11PnD

Pearson, B., B. Fox-Kemper, S. D. Bachman, and F. O. Bryan: 2017, Evaluation of scale-aware subgrid mesoscale eddy models in a global eddy-rich model. *Ocean Modelling*, **115**, 42–58. URL http://dx.doi.org/10.1016/j.ocemod.2017.05.007

Peixoto, J. P. and A. H. Oort: 1992, *Physics of Climate.*. American Institute of Physics, New York, 520pp, 520 pp.

Penney, J. and M. Stastna: 2016, Direct numerical simulation of double-diffusive gravity currents. *Physics of Fluids*, **28**, 086602.

Price, J. F., R. A. Weller, and R. Pinkel: 1986, Diurnal cycling: Observations and models of the upper ocean response to diurnal heating, cooling, and wind mixing. *Journal of Geophysical Research-Oceans*, **91**, 8411–8427.

Radko, T. and J. Marshall: 2006, The Antarctic Circumpolar Current in three dimensions. *Journal of Physical Oceanography*, **36**, 651–669.

Redi, M. H.: 1982, Oceanic isopycnal mixing by coordinate rotation. *Journal of Physical Oceanography*, **12**, 1154–1158.

Reynolds, O.: 1895, On the dynamical theory of incompressible viscous fluids and the determination of the criterion. *Philosophical Transactions of the Royal Society of London. A*, **186**, 123–164.

Rhines, P. B.: 1979, Geostrophic turbulence. Annual Review of Fluid Mechanics.

Richter, F. M.: 1986, Kelvin and the age of the Earth. *The Journal of Geology*, **94**, 395–401.

Rocha, C. B., T. K. Chereskin, S. T. Gille, and D. Menemenlis: 2016a, Mesoscale to submesoscale wavenumber spectra in Drake Passage. *Journal of Physical Oceanography*, **46**, 601–620.

Rocha, C. B., S. T. Gille, T. K. Chereskin, and D. Menemenlis: 2016b, Seasonality of submesoscale dynamics in the kuroshio extension. *Geophysical Research Letters*, **43**.

Samelson, R. M. and G. K. Vallis: 1997, A simple friction and diffusion scheme for planetary geostrophic basin models. *Journal of Physical Oceanography*, **27**, 186–194.

Schlottke, J. and B. Weigand: 2008, Direct numerical simulation of evaporating droplets. *Journal of Computational Physics*, **227**, 5215–5237.

Shevchenko, I. and P. Berloff: 2015, Multi-layer quasi-geostrophic ocean dynamics in eddy-resolving regimes. *Ocean Modelling*, **94**, 1–14.

Simmons, H., S. Jayne, L. St Laurent, and A. Weaver: 2004, Tidally driven mixing in a numerical model of the ocean general circulation. *Ocean Modelling*, **6**, 245–263.

Skyllingstad, E. D. and D. W. Denbo: 1995, An ocean large-eddy simulation of Langmuir circulations and convection in the surface mixed-layer. *Journal of Geophysical Research-Oceans*, **100**, 8501–8522.

Smagorinsky, J.: 1963, General circulation experiments with the primitive equations I: The basic experiment. *Monthly Weather Review*, **91**, 99–164.

— 1993, Some historical remarks on the use of nonlinear viscosities. *Large Eddy Simulation of Complex Engineering and Geophysical Flows*, B. Galperin and S. A. Orszag, eds., Cambridge University Press, 3–36.

Smith, K. S., G. Boccaletti, C. C. Henning, I. Marinov, C. Y. Tam, I. M. Held, and G. K. Vallis: 2002, Turbulent diffusion in the geostrophic inverse cascade.

Stacey, F. D.: 2000, Kelvin's age of the Earth paradox revisited. *Journal of Geophysical Research: Solid Earth*, **105**, 13155–13158.

Stamper, M. A. and J. R. Taylor: 2017, The transition from symmetric to baroclinic instability in the eady model. *Ocean Dynamics*, **67**, 65–80.

Stokes, G. G.: 1845, On the theories of the internal friction of fluids in motion, etc. *Trans. Camb. Philos. Soc.*, **8**, 287–319.

Stommel, H. and A. B. Arons: 1960, On the abyssal circulation of the world ocean .2. An idealized model of the circulation pattern and amplitude in oceanic basins. *Deep-Sea Research*, **6**, 217–233.

Stommel, H. M.: 1948, The westward intensification of wind-driven ocean currents. *Transactions, American Geophysical Union*, **29**, 202–206.

Straub, D. N. and B. T. Nadiga: 2014, Energy fluxes in the quasigeostrophic double gyre problem. *Journal of Physical Oceanography*, **44**, 1505–1522.

Sullivan, P. P. and J. C. McWilliams: 2018, Frontogenesis and frontal arrest of a dense filament in the oceanic surface boundary layer. *Journal of Fluid Mechanics*, **837**, 341–380.

Sullivan, P. P., J. C. McWilliams, and W. K. Melville: 2007, Surface gravity wave effects in the oceanic boundary layer: large-eddy simulation with vortex force and stochastic breakers. *Journal of Fluid Mechanics*, **593**, 405–452.

Sun, D.-Z. and Z. Liu: 1996, Dynamic ocean-atmosphere coupling: a thermostat for the tropics. *Science*, **272**, 1148–1150.

Suzuki, N. and B. Fox-Kemper: 2016, Understanding Stokes forces in the wave-averaged equations. *Journal of Geophysical Research–Oceans*, **121**, 1–18. URL http://dx.doi.org/10.1002/2015JC011566

Suzuki, N., B. Fox-Kemper, P. E. Hamlington, and L. P. Van Roekel: 2016, Surface waves affect frontogenesis. *Journal of Geophysical Research–Oceans*, **121**, 1–28. URL http://dx.doi.org/10.1002/2015JC011563

Sverdrup, H. U.: 1947, Wind-driven currents in a baroclinic ocean; with appplication to the equatorial currents of the eastern Pacific. *Proc. National Acad. Sci.*, **33**, 318–326.

Talley, L. D.: 2008, Freshwater transport estimates and the global overturning circulation: Shallow, deep and throughflow components. *Progress In Oceanography*, **78**, 257–303.

Tandon, A. and C. Garrett: 1995, Geostrophic adjustment and restratification of a mixed layer with horizontal gradients above a stratified layer. *Journal of Physical Oceanography*, **25**, 2229–2241.

Taylor, J. R. and R. Ferrari: 2010, Buoyancy and wind-driven convection at mixed layer density fronts. *Journal of Physical Oceanography*, **40**, 1222–1242.

Thomas, L. N. and C. M. Lee: 2005, Intensification of ocean fronts by down-front winds. *Journal of Physical Oceanography*, **35**, 1086–1102.

Thomas, L. N., A. Tandon, and A. Mahadevan: 2008, Submesoscale processes and dynamics. *Ocean Modelling in an Eddying Regime*, M. Hecht and H. Hasumi, eds., AGU Geophysical Monograph Series, volume 177, 17–38.

Thomas, L. N., J. R. Taylor, R. Ferrari, and T. M. Joyce: 2013, Symmetric instability in the Gulf Stream. *Deep Sea Research Part II: Topical Studies in Oceanography*, **91**, 96–110.

Trenberth, K. and J. Caron: 2001, Estimates of meridional atmosphere and ocean heat transports. *Journal of Climate*, **14**, 3433–3443.

Trenberth, K. E. and J. T. Fasullo: 2009, Changes in the flow of energy through the Earth's climate system. *Meteorologische Zeitschrift*, **18**, 369–377.

— 2010, Climate change: Tracking Earth's energy. *Science*, **328**, 316–317.

Uchiyama, Y., J. C. McWilliams, and J. M. Restrepo: 2009, Wave-current interaction in nearshore shear instability analyzed with a vortex force formalism. *Journal of Geophysical Research-Oceans*, **114**.

Vallis, G. K.: 2006, *Atmospheric and Oceanic Fluid Dynamics: Fundamentals and Large-Scale Circulation*. Cambridge University Press, Cambridge. URL http://bit.ly/SDSMSK

Van Roekel, L. P., B. Fox-Kemper, P. P. Sullivan, P. E. Hamlington, and S. R. Haney: 2012, The form and orientation of Langmuir cells for misaligned winds and waves. *Journal of Geophysical Research–Oceans*, **117**, C05001, 22pp. URL http://dx.doi.org/10.1029/2011JC007516

Veronis, G.: 1966, Wind-driven ocean circulation–Part I. Linear theory and perturbation analysis. *Deep-Sea Research*, **13**, 17–29.

Von Schuckmann, K., M. Palmer, K. Trenberth, A. Cazenave, D. Chambers, N. Champollion, J. Hansen, S. Josey, N. Loeb, P.-P. Mathieu, et al.: 2016, An imperative to monitor Earth's energy imbalance. *Nature Climate Change*, **6**, 138–144.

Wang, P., J. Sheng, and C. Hannah: 2017, Assessing the performance of formulations for nonlinear feedback of surface gravity waves on ocean currents over coastal waters. *Continental Shelf Research*.

Waterhouse, A. F., J. A. MacKinnon, J. D. Nash, M. H. Alford, E. Kunze, H. L. Simmons, K. L. Polzin, L. C. St. Laurent, O. M. Sun, R. Pinkel, et al.: 2014, Global patterns of diapycnal mixing from measurements of the turbulent dissipation rate. *Journal of Physical Oceanography*, **44**, 1854–1872.

Webb, A. and B. Fox-Kemper: 2011, Wave spectral moments and Stokes drift estimation. *Ocean Modelling*, **40**, 273–288.

Webb, A. and B. Fox-Kemper: 2015, Impacts of wave spreading and multidirectional waves on estimating Stokes drift. *Ocean Modelling*, **96**, 49–64. URL http://dx.doi.org/10.1016/j.ocemod.2014.12.007

Whitt, D. B. and J. R. Taylor: 2017, Energetic submesoscales maintain strong mixed layer stratification during an autumn storm. *Journal of Physical Oceanography*, **47**, 2419–2427.

Wunsch, C. and R. Ferrari: 2004, Vertical mixing, energy and the general circulation of the oceans. *Annual Review of Fluid Mechanics*, **36**, 281–314.

Wunsch, C. and D. Roemmich: 1985, Is the North Atlantic in Sverdrup balance? *Journal of Physical Oceanography*, **15**, 1876–1880.

Yeager, S.: 2015, Topographic coupling of the Atlantic overturning and gyre circulations. *Journal of Physical Oceanography*, **45**, 1258–1284.

Young, W. R.: 2010, Dynamic enthalpy, conservative temperature, and the seawater Boussinesq approximation. *Journal of Physical Oceanography*, **40**, 394–400.